Marvi-Mashhadia, M.; Rodríguez-Martínez, J. A. Multiple necking patterns in elasto-plastic rings subjected to rapid radial expansion: The effect of random distributions of geometric imperfections, In *International Journal of Impact Engineering, 144, Oct. 2020, 103661, 17 pp.*

DOI: https://doi.org/10.1016/j.ijimpeng.2020.103661

Multiple necking patterns in elasto-plastic rings subjected to rapid radial expansion: The effect of random distributions of geometric imperfections

M. Marvi-Mashhadi, J. A. Rodríguez-Martínez*

Department of Continuum Mechanics and Structural Analysis. University Carlos III of Madrid. Avda. de la Universidad, 30. 28911 Leganés, Madrid, Spain

Abstract

In this paper we have investigated, using finite element calculations performed in ABAQUS/Explicit [1], the effect of *ab initio* geometric imperfections in the development of multiple necking patterns in ductile rings subjected to dynamic expansion. Specifically, we have extended the work of Rodríguez-Martínez et al. [33], who studied the formation of necks in rings with sinusoidal spatial perturbations of predefined amplitude and constant wavelength, by considering specimens with random distributions of perturbations of varying amplitude and wavelength. The idea, which is based on the work of El Maï et al. [4], is to provide an idealized modeling of the surface defects and initial roughness of the rings and explore their effect on the collective behavior and spacing of the necks. The material behavior has been modeled with von Mises plasticity and constant yield stress, and the finite element simulations have been performed for expanding velocities ranging from 10 m/s to 1000 m/s, as in ref. [33]. For each speed, we have performed calculations varying the number of imperfections in the ring from 5 to 150. In order to obtain statistically significant results, for each number of imperfections, the computations have been run with five random distributions of imperfection wavelengths. For a small number of imperfections, the variability in the wavelengths distribution is large, which makes the imperfections play a major role in the necking pattern, largely controlling the spacing and growth rate of the necks. As the number of imperfections increases, the variability in the wavelengths distribution decreases, giving rise to an array of more regularly spaced necks which grow at more similar speed. A key outcome is to show that, for a large number of imperfections, the number of necks formed in the ring comes closer to the number of necks obtained in the absence of *ab initio* geometric imperfections.

Keywords:

Ring expansion, Finite elements, Multiple necking, Geometric imperfections, Inertia, Stress multiaxiality

*Corresponding author. Tel. +34 916249904; Fax: +33 916249430. E-mail address: jarmarti@ing.uc3m.es

1. Introduction

The effect of material and geometric imperfections in the fragmentation of metallic structures subjected to dynamic loading has been the subject of recurrent debate within the Solid Mechanics community for more that 70 years. In the 40's of the last century, Mott [26, 24, 22, 23, 25] published what is still considered as a reference model to explain the basic physical mechanisms underlying dynamic fragmentation of ductile materials. The theory of Mott, that was primarily developed during World War II to describe the process of fragmentation resulting from the explosive rupture of cylindrical shell casings, is basically a statistical one-dimensional model that considers the onset of fractures as a random process that responds to the inherent variability of the fracture strain of metallic materials. The underlying idea is that the fragmentation occurs due to the activation of weak points of the material, such as defects or geometric imperfections, which are distributed throughout the specimen and lead to the formation of multiple necks (in ductile materials) which eventually develop into fractures. The distribution of neck spacings and fragment sizes is determined by the propagation of the unloading waves which emanate from each necked and fracture site, and lead to the development of obscured (unloaded) zones in which additional necks cannot nucleate and fractures cannot occur.

The original theory of Mott [26, 24, 22, 23, 25] was extended years later by Grady and collaborators [10, 17, 8, 11] to account for the dissipation of energy associated with the fracture process. These authors derived expressions for the nominal fragment size, fracture time, and dynamic fracture strain that found reasonable agreement with experiments and numerical computations, e.g. refs. [17, 18, 11]. Indeed, with the development of Computational Mechanics, the finite element method has been extensively used over the last 3 decades to simulate multiple necking and dynamic fragmentation problems, e.g. refs. [13, 39, 31, 36, 12, 40, 34, 33]. The popularity of computer simulations to study fragmentation problems is partly due to the elevated cost of fragmentation experiments, and the fact that there are only a few laboratories in the world with the equipment and skills required to perform such tests (e.g. high-velocity expansion of ring [28, 9, 2, 47, 15, 3], thin-walled cylinders [35, 14, 7, 48, 16] and hemispherical shells [19]). In addition, the finite element calculations have the potential to provide information about the mechanisms which control multiple necking and fragmentation that is not accessible by experimentation.

For instance, finite element simulations have been extremely useful to obtain insights into the role of geometric imperfections on the dominant and arrested necks, the fragmentation patterns, and the distribution of fragment sizes. Namely, Han and Tvergaard [13] analyzed using 2D numerical simulations the formation of multiple necks in plane-strain cylinders expanding dynamically under prescribed body forces. The material, considered rate and temperature independent, was described using von Mises plasticity and isotropic hardening. The authors included in the specimen an array of sinusoidal geometric imperfections to break the symmetry of the problem and trigger necking localization. They showed that, due to inertia effects, multiple necks can be formed at locations other than the prescribed initial thickness imperfections. Sørensen and Freund [36] studied numerically the formation and growth of necks in thin-walled metal tubes undergoing high-rate radial expansion under plane strain conditions. The necking pattern was triggered including in the finite element model sinusoidal periodic imperfections of constant wavelength and amplitude. A main difference with previous work of Han and Tvergaard [13] is that the plastic behaviour of the material was described using Gurson plasticity, taking into account the nucleation and growth of microvoids, and the temperature and strain rate sensitivities of the material. These authors showed that, for long wavelength imperfections of small amplitude, an array of *regularly spaced necks* appeared around the circumference of the ring. As in the numerical results of Han and Tvergaard [13], the spacing of the necks showed little correlation with the initial imperfections distribution. Moreover, Guduru and Freund [12] simulated in ABAQUS/Explicit [1] the ring expansion experiments performed by Grady and Benson [9] with $1100-0$ aluminum and OFHC copper specimens. As in Sørensen and Freund [36], the material was modeled with Gurson plasticity, and fracture was considered to occur when a critical value of porosity was reached. The finite element model consisted of a long cylindrical bar subjected to dynamic stretching and with initial conditions consistent with the expanding ring. The authors performed calculations in which the radius of the bar was given a small sinusoidal geometric imperfection and showed, consistently with the results of Han and Tvergaard [13] and Sørensen and Freund [36] for long wavelength imperfections, that the amplitude of the imperfection had no significant influence on the number of necks and fragments. The authors also noted that in ABAQUS/Explicit [1], unlike in the in-house code used by Han and Tvergaard [13], no imperfection is needed to trigger the formation of necks, since the numerical perturbations introduced by the software are sufficient to cause the instability when the critical conditions are reached. The finite element results obtained with and without geometric imperfection found reasonable agreement with the experiments of Grady and Benson [9] for the number of necks and the fragmentation statistics. The numerical calculations were also compared with a linear stability analysis which provided accurate predictions for the increase in the number of necks with the extension velocity. The linear stability analysis suggested that the suppression of both short and long necking wavelengths due to stress multiaxiality (i.e. triaxiality) and inertia, respectively, favors the growth of an intermediate necking wavelength which determines the average size of the necks at high loading velocities [5, 6, 20, 21]. Moreover, Rodríguez-Martínez et al. [33] performed finite element simulations with ABAQUS/Explicit [1] of the dynamic expansion of rings with periodic geometric imperfections of constant amplitude and wavelength. The main difference with previous works of Han and Tvergaard [13], Sørensen and Freund [36] and Guduru and Freund [12] is that Rodríguez-Martínez et al. [33] explored a wider range of imperfection wavelengths such that the number of imperfections included in the ring was varied from 5 to 150 (i.e. from short to long wavelength imperfections). The finite element calculations of Rodríguez-Martínez et al. [33] confirmed the linear stability analysis predictions reported in refs. [5, 6, 12, 20, 21]: while for intermediate wavelength imperfections every imperfection evolved into a neck, for short and long wavelength imperfections the necking pattern showed little correlation with the imperfections distribution. The suppression of short and long wavelength imperfections led to the emergence of a dominant necking pattern with the same average spacing obtained in finite element calculations in which no geometric imperfection was included (and the necking pattern was triggered by the numerical perturbations introduced by the software).

In this paper we extend the finite element analyses of Han and Tvergaard [13], Sørensen and Freund [36], Guduru and Freund [12] and Rodríguez-Martínez et al. [33] by considering expanding rings with random distributions of geometric imperfections of varying amplitude and wavelength. As in ref. [33], the material is modeled with von Mises plasticity and constant yield stress. The numerical calculations are performed in ABAQUS/Explicit [1] for expanding velocities ranging from 10 m/s to 1000 m/s. For each speed, we have performed calculations varying the number of imperfections in the ring from 5 to 150. In order to obtain statistically significant results, for each number of imperfections, the computations have been run with five random distributions of imperfection wavelengths. The finite element results are compared with: (i) the calculations reported by Rodríguez-Martínez et al. [33] for rings with imperfections of constant amplitude and wavelength, (ii) the numerical simulations performed by Guduru and Freund [12] with ABAQUS/Explicit [1] for stretching bars in which the necking pattern is triggered by the numerical perturbations of the software, (iii) the predictions of a one-dimensional linear stability analysis developed by N'souglo et al. [30] (which is based on the earlier work of Zhou et al. [50]) and (iv) the experiments of Grady and Benson [9] with $1100-0$

aluminum and OFHC copper rings. The finite element calculations performed in this paper show that, if the variability in the wavelengths of the perturbations is large (small number of imperfections), both number and growth rate of the necks are mostly controlled by the imperfections. However, if the variability in the wavelengths of the perturbations is small (large number of imperfections), the number of necks obtained in the finite element simulations show qualitative and quantitative agreement with the results obtained in refs. [33, 12, 30, 9].

2. Finite element model

This section describes the 3D finite element model developed in ABAQUS/Explicit [1] to study the effect of geometric imperfections on the formation of multiple necks in ductile rings subjected to dynamic radial expansion.

The model, shown in Fig. 1, is based on previous works, see refs. [34, 41, 33]. Material points are referred to using a Cartesian coordinate system with positions in the reference configuration denoted as $\{X, Y, Z\}$. The origin of the coordinate system is located at the center of mass of the specimen. The ring is considered to have a constant inner radius and variable radial thickness in the initial configuration, with the outer radius being defined by an array of N sinusoidal imperfections with varying amplitude and wavelength (the imperfections are also called *geometric perturbations* everywhere in this paper). Motivated by the recent work of El Maï et al. [4], the goal is to provide an idealized modeling of the surface defects and initial roughness of the ring and explore their effect on the collective behavior and spacing of the necks. The wavelengths of the imperfections are generated using a Gaussian probability density function:

$$\sum_{n=1}^{N} 2 n_i \pi R_{ext} = \sum_{n=1}^{N} \lambda_i \tag{1}$$

where $R_{ext} = 16$ mm is the maximum outer radius of the ring (i.e. the radius without imperfection), n_i is the random number $\in (0, 1)$ with $\sum_{n=1}^{N} n_i = 1$, and λ_i is the wavelength of the i-th imperfection. We have generated five random distributions of imperfection wavelengths denoted as RDIW$_i$ with $i = 1, ..., 5$. Fig. 2 shows histograms with the number of imperfections N as a function of the wavelength of the imperfections λ. The results corresponding to RDIW$_2$ (black blocks) and RDIW$_3$ (red blocks) are included in each histogram. For $N = 10$, Fig. 2(a), the distribution of wavelengths is very heterogeneous with values of λ ranging between 1.7 mm and 21.6 mm, being the average wavelength $\lambda_{\text{avg}} \approx 10$ mm. The variability in the wavelengths distribution is gradually reduced as the number of imperfections increases. For instance, for $N = 50$ and $N = 100$, Figs. 2(b) and 2(c), the span of wavelengths is 0.004 mm $\leq \lambda \leq 4.84$ mm and 0.002 mm $\leq \lambda \leq 2.09$ mm, respectively. Notice that the average wavelength of the imperfections for $N = 50$ and 100 is $\lambda_{\text{avg}} \approx 2$ mm and ≈ 1 mm, respectively.

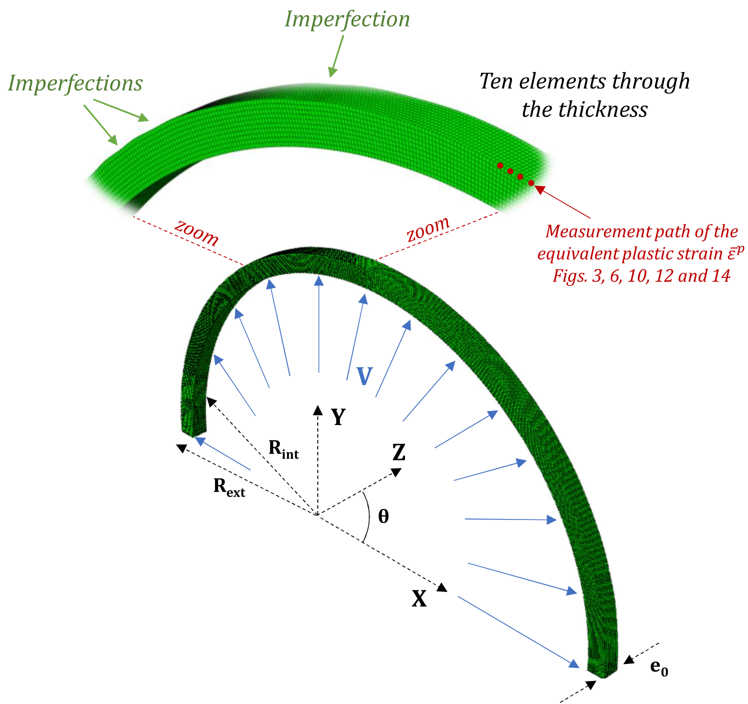

Figure 1: Finite element model. Mesh, geometry and boundary conditions. Note that, due to the symmetry of the specimen, only half of the ring is shown. The number of imperfections is $N = 40$ and the amplitude of the imperfections is $\delta = 0.01$ mm.

Moreover, the inner radius and the axial thickness of the ring are $R_{int} = 15$ mm and $e_0 = 1$ mm, respectively (see Fig. 1). These dimensions are taken from Rodríguez-Martínez et al. [33], and they are similar to those used in the experiments of Grady and Olsen [11] and Zhang and Ravi-Chandar [47]. The X and Y coordinates of the outer perimeter of the ring are calculated as:

$$X = \left\{ R_{ext} - \frac{\delta_i}{2} \Big[1 - \cos\left(\frac{2\pi R_{ext}\theta}{\lambda_i} \right) \Big] \right\} \Big[\cos(\theta) \Big] \tag{2a}$$

$$Y = \left\{ R_{ext} - \frac{\delta_i}{2} \Big[1 - \cos\left(\frac{2\pi R_{ext}\theta}{\lambda_i} \right) \Big] \right\} \Big[\sin(\theta) \Big] \tag{2b}$$

where δ_i is the amplitude of the i-th imperfection and θ is the radial angle, see Fig. 1. Let us denote by

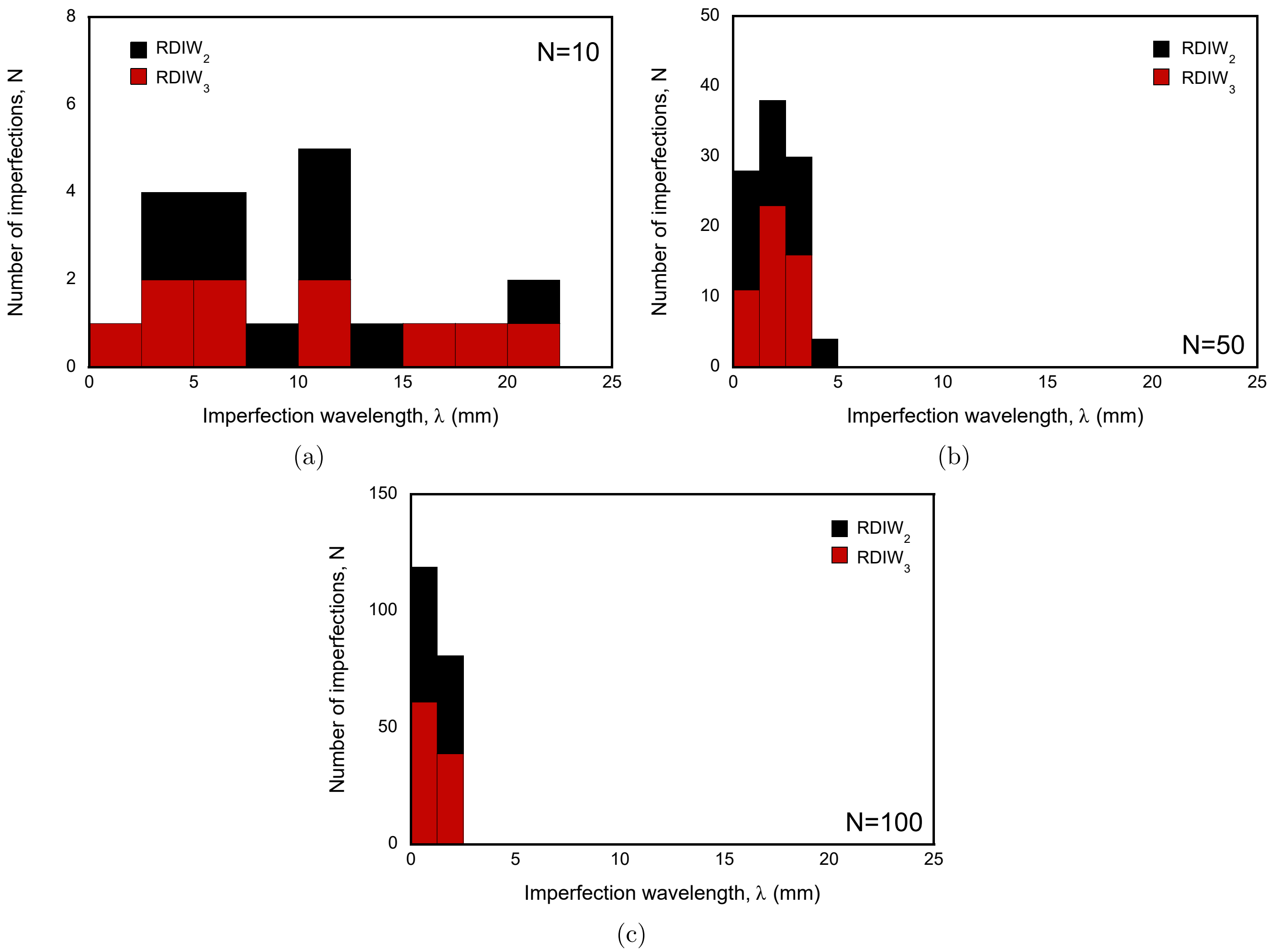

Figure 2: Histograms showing the number of imperfections N as a function of the imperfection wavelength λ. Results are presented for two different random distributions of imperfection wavelengths: RDIW_2 (black blocks) and RDIW_3 (red blocks). The height of a colored block within a bar of the histogram marks the number of imperfections within a fixed λ interval for a given distribution of imperfection wavelengths. Results are shown for different number of imperfections: (a) $N = 10$, (b) $N = 50$ and (c) $N = 100$. For interpretation of the references to color in the text, the reader is referred to the web version of this article.

$\theta_i = \lambda_i / R_{ext}$ the radial angle of the i-th imperfection with wavelength λ_i. By inserting λ_i in equations (2a) and (2b), while increasing θ from θ_i to θ_{i+1}, we obtain the X and Y coordinates corresponding to the imperfection with wavelength λ_i. Repeating the same process for all the other λ_i provides the coordinates of the N imperfections included in the model. Moreover, the amplitude of the i-th imperfection is a random number within the range 0.005 mm $\leq \delta_i \leq$ 0.025 mm that has also been generated with a Gaussian probability density function. These imperfection amplitudes lie within the typical values for the surface roughness obtained in sintered and additively manufactured parts, e.g. see refs. [38, 37]. Note that we have generated 1000 pairs of X and Y coordinates to obtain an accurate description of the sinusoidal profile of the outer perimeter of the ring.

The loading condition is a radial velocity, V_r, applied in the inner surface of the ring which remains constant throughout the entire analysis [34, 41, 32, 33]. The initial condition is a radial velocity of the same value $V(t = 0) = V_r$ applied to all the nodes of the finite element mesh. The application of this initial condition is essential to minimize the propagation of waves through the thickness of the ring due to the abrupt motion of the inner face at $t = 0$ while the reminder of the specimen is initially at rest. Otherwise, for sufficiently high loading velocities, the waves generated due to the application of the loading condition could lead to instantaneous flow localization in the inner surface of the specimen [27, 45]. The initial strain rate in the material is $\dot{\varepsilon}_0 = V_r / R_{int}$. As in Rodríguez-Martínez et al. [33], the material behavior is modeled using linear isotropic elasticity, with Young modulus $E = 200$ GPa and Poisson's ratio $\nu = 0.3$, and von Mises plasticity with associated flow rule and constant yield stress $\sigma_y = 500$ MPa (i.e., the material is considered elastic, perfectly plastic). The initial material density is $\rho = 7800$ kg/m^3. We are aware that the constitutive model considered in this work, that neglects the effects of strain, strain rate and temperature in the plastic response of the material, is an idealization of the actual behavior of most metals and alloys. However, using this *simple* constitutive model has the advantage of reducing the factors that control the formation and development of the necking pattern in the simulations presented in Section 3 to only three: inertia, stress multiaxiality (i.e. triaxiality) and geometric imperfections. This facilitates the interpretation of the results and thus the identification of the role played by the geometric imperfections in the localization process. Furthermore, we think that the overall trends and conclusions obtained in this paper are still valid for actual materials with flow stress dependent on strain, strain rate and temperature. On other hand, previous works reported in the literature suggested that strain hardening delays necking formation [20], the strain rate hardening increases the necking strain and the average spacing between necks [21], and the thermal softening promotes early formation of necks and leads to the decrease of the distance between consecutive necks [46]. Nevertheless, determining to which amount strain, strain rate and temperature affect the necking pattern at high strain rates, when inertia effects are important, still requires further research. Note that the calculations reported in refs. [36, 32, 30] showed that at sufficiently high strain rates the number of necks, and the average spacing between consecutive necks, is generally not very sensitive to the material properties, which may indicate that inertia is a main factor controlling the necking pattern. Nevertheless, this conclusion still needs further research.

The ring has been discretized using ≈ 100000 tri-linear elements with 8-nodes and reduced integration (C3D8R in ABAQUS notation [1]). We have used variable size elements to ensure the quality of the mesh for the smallest imperfection wavelengths (which in some cases are of the order of few tens of microns) such that the specific number of elements slightly varies ($\pm 10\%$) with the number and distribution of imperfections. Ten elements are included through the thickness of the ring. A mesh convergence study has been performed, in which the time evolution of the strain field in the specimen, and the number of necks incepted, were compared for different mesh sizes. There is some mesh sensitivity in the numerical calculations, however it does not affect significantly the finite element results presented in this paper, neither quantitatively nor qualitatively (see Appendix A). The mesh design of the ring with $N = 40$ and $\delta = 0.01$ mm is shown in Fig. 1.

3. Results

Sections 3.1 and 3.2 show finite element results for simulations with imperfections of constant and varying amplitude, respectively. The calculations have been performed for expanding velocities ranging from 10 m/s to 1000 m/s, as in ref. [33]. Inertia effects can be quantified with the dimensionless number $\bar{I} = \sqrt{\frac{\rho (R_{ext}-R_{int})^2 \dot{\varepsilon}_0^2}{\sigma_y}}$, which is derived from the balance of linear momentum [50]. For the calculations performed in this paper, $\bar{I}$ varies from 0.0026 for $V_r = 10$ m/s to 0.26 for $V_r = 1000$ m/s. The finite element simulations reported in refs. [32, 29, 49] suggested that the role of inertia effects on necks spacing is especially relevant for $\bar{I} \gtrsim 0.06-0.1$, when the necking strain corresponding to the critical necking wavelength (also called critical neck size) becomes significantly smaller than for any other necking wavelength. While the largest velocities considered in this paper exceed the regular experimental capabilities (ring expansion tests can rarely be performed for velocities higher than 300 m/s, see Grady and Olsen [11] and Zhang and Ravi-Chandar [47]), exploring such a wide range of loading rates helps to enlighten the role of geometric imperfections on the formation of multiple necking patterns. For each expansion velocity, we have performed calculations varying the number of imperfections in the ring from 5 to 150. Notice that the variability in the distribution of imperfection wavelengths decreases as N increases (see Fig. 2). In order to obtain statistically significant results, for each number of imperfections, the computations have been run with five random distributions of imperfection wavelengths (as mentioned in Section 2). We have also performed calculations with $N = 0$ for which, in absence of geometric defects, the necking pattern is triggered by the numerical perturbations introduced by the software [34, 32, 42].

3.1. Constant amplitude imperfections

Fig. 3 shows the normalized equivalent plastic strain $\hat{\bar{\varepsilon}}^p$ versus the normalized outer perimeter of the ring $\hat{P} = \dfrac{\theta}{2\pi}$ for calculations with imposed initial strain rate $\dot{\varepsilon}_0 = 16667\ \mathrm{s}^{-1}$ (which corresponds to $V_r = 250$ m/s). The results correspond to the cases with $N = 0, 10, 50$ and 100. Recall that for $N = 0$ no imperfections are included in the ring. For $N = 10, 50$ and 100 the amplitude of the imperfections is $\Delta = \dfrac{\delta}{R_{ext} - R_{int}} \times 100 = 1\%$ and the random distribution of imperfection wavelengths is RDIW$_1$. The normalized equivalent plastic strain is defined as $\hat{\bar{\varepsilon}}^p = \dfrac{\bar{\varepsilon}^p}{\bar{\varepsilon}^p_b}$, where $\bar{\varepsilon}^p$ is the equivalent plastic strain measured in the outer surface of the specimen along the path shown in Fig. 1. Moreover, $\bar{\varepsilon}^p_b = \ln\left(\dfrac{R_{ext} + V_r\, t}{R_{ext}}\right)$ approximates the background equivalent strain in the ring (the background strain corresponds to the fundamental solution of the problem in absence of imperfections and before necking localization [42]). Therefore, before the necking pattern is formed, the normalized equivalent plastic strain is ≈ 1. The $\hat{\bar{\varepsilon}}^p - \hat{P}$ curves shown in Fig. 3 display a succession of peaks and valleys. Similarly to N'souglo et al. [30] and Vaz-Romero et al. [42], we consider that necks are all the excursions of strain that fulfill the condition $\hat{\bar{\varepsilon}}^p = 1.1$ when the maximum value of $\hat{\bar{\varepsilon}}^p$ reaches ≈ 2.5. This criterion has been chosen such that the necking pattern is generally formed, yet the strains are not so large that the finite element grid becomes excessively distorted. The results reported in Appendix B show that the number of necks is not generally very sensitive to the precise cut-off values chosen, i.e. the trends and conclusions presented in this paper remain essentially the same for different necking criteria. Nevertheless, this necking criterion has some limitations, as shown below in this paper (see Figs. 9 and 12). Moreover, note that Fig. 3 shows results only for values of $\hat{P}$ ranging from 0 to 0.5, i.e., the results correspond to an angular section of 180°. Displaying 50% of the perimeter of the ring allows to include enough necks to obtain a representative sample of the entire localization pattern, without impairing the clarity of the graph.

Fig. 3(a) shows the results for $N = 0$ and three different loading times: $t = 5$ μs, 55 μs and 69 μs. Note that the three $\hat{\bar{\varepsilon}}^p - \hat{P}$ curves intersect with each other several times. If the $\hat{\bar{\varepsilon}}^p - \hat{P}$ curve is shifted upwards with increasing time (e.g., the dashed green curve $t = 69$ μs is above the solid red curve $t = 55$ μs) is that the equivalent plastic strain $\bar{\varepsilon}^p$ has increased more than the background strain $\bar{\varepsilon}^p_b$ at the corresponding material point, which indicates the development of the localization process. Similarly, if increasing the loading time shifts the $\hat{\bar{\varepsilon}}^p - \hat{P}$ curve downwards (e.g., the dashed green curve is below the solid red curve) is that the material is unloading elastically (see also Vaz-Romero et al. [42]). For $t = 5$ μs the normalized equivalent plastic strain is *virtually* constant (the fluctuations of the equivalent strain are not noticeable in the graph), meaning that the strain field in the specimen is largely homogeneous and localization has not occurred yet. For $t = 55$ μs the maximum normalized equivalent plastic strain reaches ≈ 1.5. There is a series of peaks and valleys which illustrate the incipient formation of a localization pattern. For $t = 69$ μs the maximum value of $\hat{\bar{\varepsilon}}^p$ is ≈ 2.5. Attending to the necking criterion defined in previous paragraph (necks are the excursions of strain that fulfill the condition $\hat{\bar{\varepsilon}}^p = 1.1$ when the maximum value of $\hat{\bar{\varepsilon}}^p$ reaches ≈ 2.5), there are 18 necks in the graph which are indicated with blue numbers. There is also an excursion of strain indicated with an orange arrow that has been arrested before reaching the necking criterion. The localization pattern is illustrated in the equivalent plastic strain contours of Fig. 4(a) which show multiple necks in which the plastic strain reaches values above 0.75. Note that, due to the stabilizing role of inertia [43], the plastic strain outside the necks reaches values as high as 0.5 (in absence of inertia, a rate-independent material with no strain hardening develops *instantaneous* necking localization). Moreover, the contours of stress triaxiality σ_h presented in Fig. 5(a) show that hydrostatic stresses develop in the necked zones, leading to values of σ_h greater than 0.5. The increase of triaxiality stabilizes the growth of short necks [5, 20, 32, 44], and regularizes the localization process.

Fig. 3(b) displays the results with 10 imperfections. For $t = 5$ μs, unlike in the case of $N = 0$, there are strain fluctuations caused by the geometric imperfections. These fluctuations evolve with time, giving rise to a number of strain excursions. Note that the maximum normalized equivalent plastic strain reaches 1.5 and 2.5 at $t = 13$ μs and 19 μs, respectively, much earlier than in the case of $N = 0$. Moreover, both the spacing and the growth rate of the necking pattern are more irregular than in the case of $N = 0$. There are 6 necks in the graph, 2 of them growing much faster than the others. These two main necks (3 and 6), which can be seen in the equivalent plastic strain contours of Fig. 4(b), create disturbances in the strain field that lead to the formation of additional necks (2, 4 and 5). These results show a great resemblance with the finite element simulations of Vaz-Romero et al. [43] for nonlinear elastic bars subjected to dynamic stretching and with initial conditions consistent with the expanding ring. These authors showed that including a spatial-localized defect in the homogeneous strain rate field of the bar leads to the activation of additional instability modes (additional to the mode of the strain rate defect) which trigger the formation of multiple necks (see Fig. 9 in ref. [43]). The activation of these additional instability modes is due to inertia effects, which also control (to some extent) the number and size of the modes activated. Moreover, notice in Fig. 4(b) that the value of the equivalent plastic strain outside the necked zones, which correspond to the valleys in Fig. 3(b), is ≈ 0.13, i.e. approximately 3.75 times smaller than in the case of $N = 0$ (the imperfections favor early necking). Moreover, Fig. 5(b) shows that the stress triaxiality near the two main necks is significantly higher that in the rest of the specimen, where it is approximately 1/3.

Fig. 3(c) shows the results for $N = 50$ and three loading times: $t = 5$ μs, 17 μs and 21 μs. The excursions of strain at $t = 5$ μs are located at the sites of minimum thickness and they grow at rates *comparable* to the rate of the background strain. As the loading time evolves, some of these excursions further develop (growing faster than the background strain), some other merge, and the rest are arrested. The combined effects of inertia and stress multiaxiality (see Fig. 5(c)), and the wave disturbances emanating from the evolving necks, control the formation and evolution of the localization pattern [43]. At $t = 17$ μs, for which the maximum normalized equivalent strain is ≈ 1.5, there are less *peaks* than at $t = 5$ μs. The arrested excursions of strain are marked with orange arrows. At $t = 21$ μs, the number of necks is 14, eight more that in the case of $N = 10$. Note also that the spacing and growth rate of the necks is more regular. Fig. 4(c) shows the equivalent plastic strain contours with the array of necks located along the perimeter of the specimen. The average value of the equivalent plastic strain outside the necks is ≈ 0.12, similar to the case of $N = 10$.

Fig. 3(d) presents the results for 100 imperfections. The comparison of the $\hat{\bar{\varepsilon}}^p - \hat{P}$ curves for $t = 5$ μs, 21 μs and 29 μs illustrates the initiation and development of the necking pattern. The time 5 μs corresponds to an early stage of the loading process so that all the strain peaks are located at the sites of minimum thickness. At $t = 21$ μs, the maximum normalized equivalent plastic strain $\hat{\bar{\varepsilon}}^p$ reaches 1.5, and the number of strain excursions has been already considerably reduced. At $t = 29$ μs, for which the maximum normalized equivalent plastic strain reaches 2.5, there are 15 excursions of strain indicated with blue numbers that fulfill the necking criterion. The locations of these necks only show partial correlation with the imperfections distribution. Notice that the number of necks becomes similar to the case for which the localization pattern was triggered by the numerical perturbations of the software ($N = 0$), indicating that as N increases the effect of the imperfections in the necking pattern is gradually reduced (as further discussed in Fig. 8). Notice also that the loading time required to reach the necking criterion seems to increase with N, and the spacing and growth rate of the necks tend to be more uniform. The case $N = 10$ shows the greater variability in the distribution of imperfections wavelength, and thus the most irregular localization pattern. The cases $N = 0$ (no *ab initio* imperfection), $N = 50$ and $N = 100$ show *more similar* necking pattern (in terms of number and growth rate of necks) because for large N, the variability in the distribution of imperfections wavelength is small, and thus, the results seem to approach the case for which no imperfections are included. The contours of equivalent plastic strain shown in Fig. 4(d) for $t = 29$ μs illustrate the array of necks formed in the ring. The equivalent plastic strain outside the necks is ≈ 0.18, approximately 30% greater than in the cases of $N = 10$ and $N = 50$. The stress triaxiality contours of Fig. 5(d) show that inside the necked zones the stress triaxiality reaches values beyond 0.5, i.e. significantly greater than the triaxiality corresponding to uniaxial tension 1/3.

Fig. 6 shows a comparison between the $\hat{\bar{\varepsilon}}^p - \hat{P}$ curves obtained for two random distributions of imperfection wavelengths: RDIW$_2$ and RDIW$_3$. As in Fig. 3, the results correspond to half of the perimeter of the ring, $0 \leq \hat{P} \leq 0.5$. The imposed initial strain rate and the amplitude of the geometric imperfections are $\dot{\varepsilon}_0 = 16667$ s^{-1} (i.e. $V_r = 250$ m/s) and $\Delta = 1\%$, respectively. The results correspond to the loading times for which the maximum value of $\hat{\bar{\varepsilon}}^p$ reaches ≈ 2.5.

Fig. 6(a) shows the results for $N = 10$. The loading time for both imperfection distributions is $t = 19$ μs. The necks for RDIW$_2$ and RDIW$_3$ are indicated with blue and orange numbers, respectively. Similarly to the results shown for RDW$_1$ in Fig. 3(b), there is an important variability in the growth rate of the necks. Notice also that the specific location of the necks depends on the imperfections distribution. The necks 4 and 2 corresponding to the distributions RDIW$_2$ and RDIW$_3$, respectively, grow faster and create perturbations

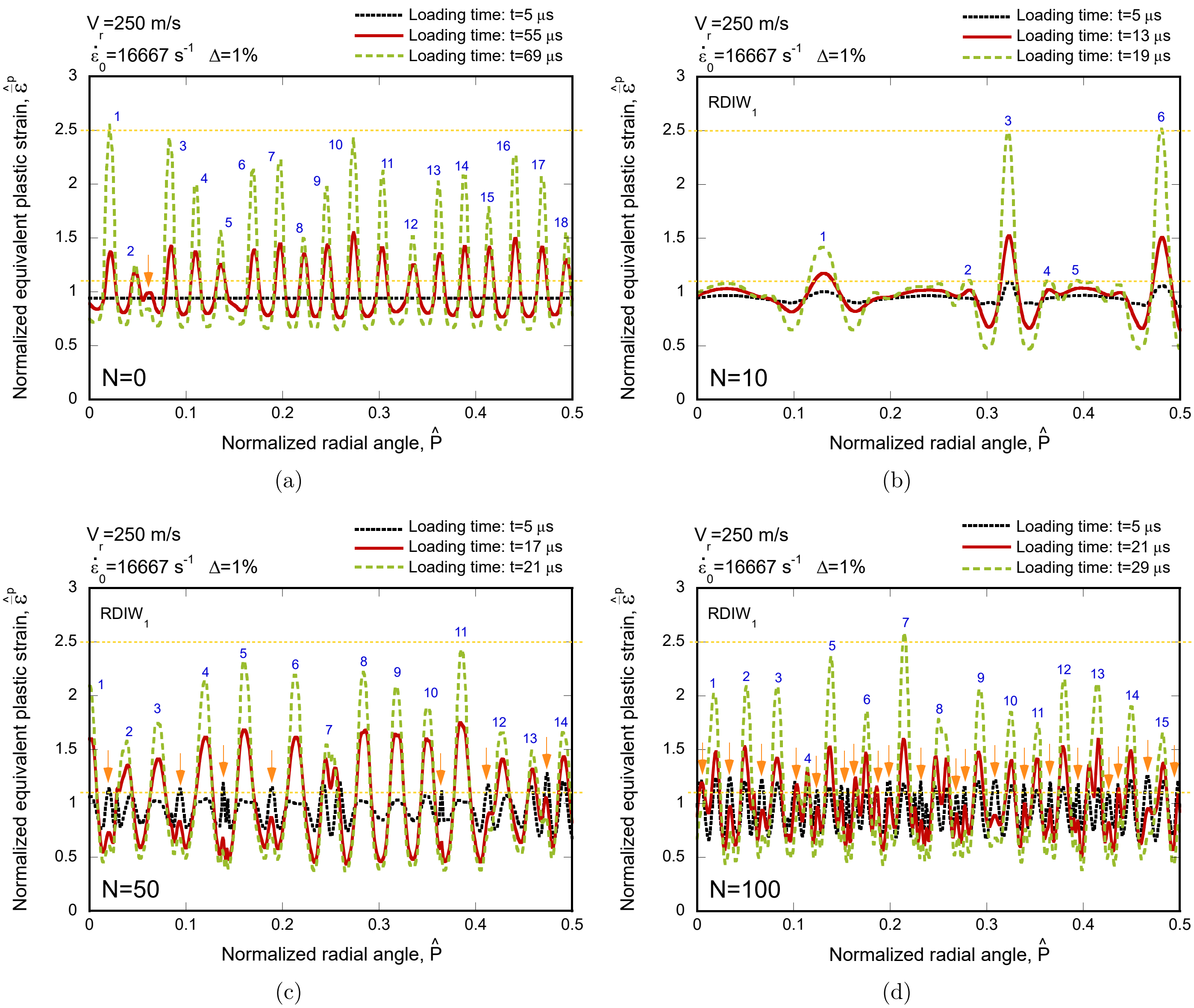

Figure 3: Normalized equivalent plastic strain $\hat{\bar{\varepsilon}}^p$ versus normalized outer perimeter of the ring $\hat{P}$. Imposed initial strain rate of $\dot{\varepsilon}_0 = 16667\ \text{s}^{-1}$ (which corresponds to $V_r = 250$ m/s). (a) Number of imperfections $N = 0$. Three loading times t are considered: 5 μs, 55 μs and 69 μs. (b) Number of imperfections $N = 10$. Three loading times t are considered: 5 μs, 13 μs and 19 μs. (c) Number of imperfections $N = 50$. Three loading times t are considered: 5 μs, 17 μs and 21 μs. (d) Number of imperfections $N = 100$. Three loading times t are considered: 5 μs, 21 μs and 29 μs. For $N = 10, 50$ and 100 the amplitude of the imperfections is $\Delta = 1\%$ and the random distribution of imperfection wavelengths is RDIW$_1$. The horizontal yellow dashed lines correspond to the conditions $\hat{\bar{\varepsilon}}^p = 1.1$ and $\hat{\bar{\varepsilon}}^p = 2.5$. For interpretation of the references to color in this figure, the reader is referred to the web version of this article.

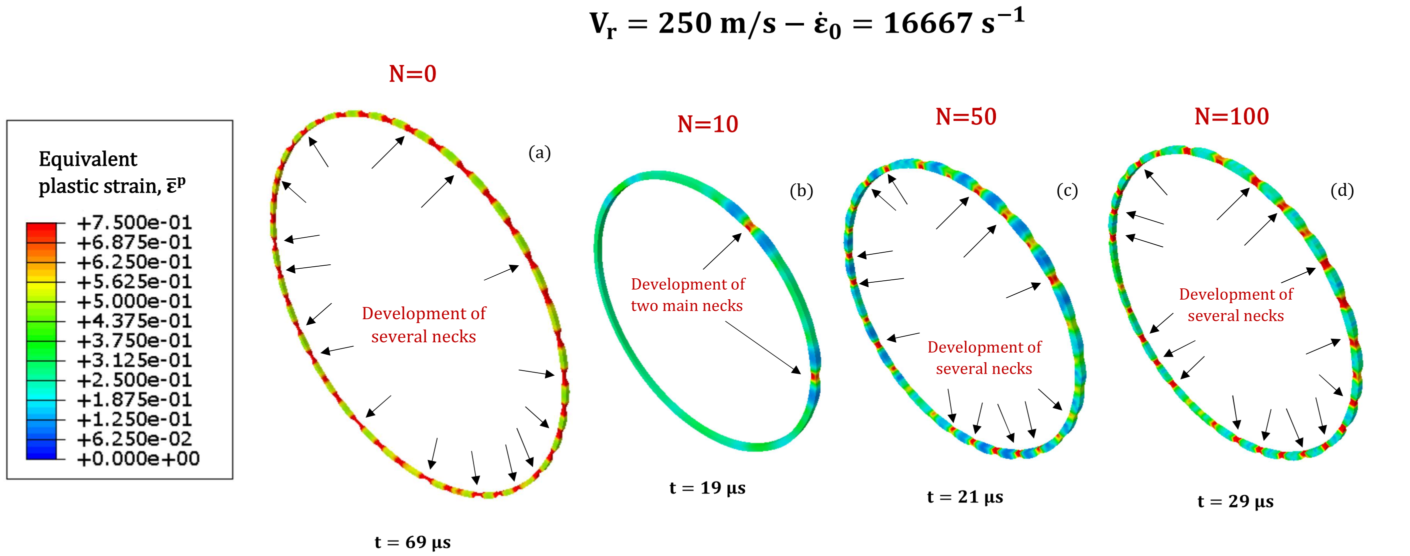

Figure 4: Contours of equivalent plastic strain $\bar{\varepsilon}^p$. Imposed initial strain rate of $\dot{\varepsilon}_0 = 16667$ s^{-1} (which corresponds to $V_r = 250$ m/s). (a) Number of imperfections $N = 0$. Loading time $t = 69$ μs. (b) Number of imperfections $N = 10$. Loading time $t = 19$ μs. (c) Number of imperfections $N = 50$. Loading time $t = 21$ μs. (d) Number of imperfections $N = 100$. Loading time $t = 29$ μs. For $N = 10, 50$ and 100 the amplitude of the imperfections is $\Delta = 1\%$ and the random distribution of imperfection wavelengths is RDIW$_1$. All the isocontours have the same colour coding such that equivalent plastic strains ranging from 0 to 0.75 correlate with a colour scale that goes from blue to red. If the value of the equivalent plastic strain is above 0.75, it remains red.

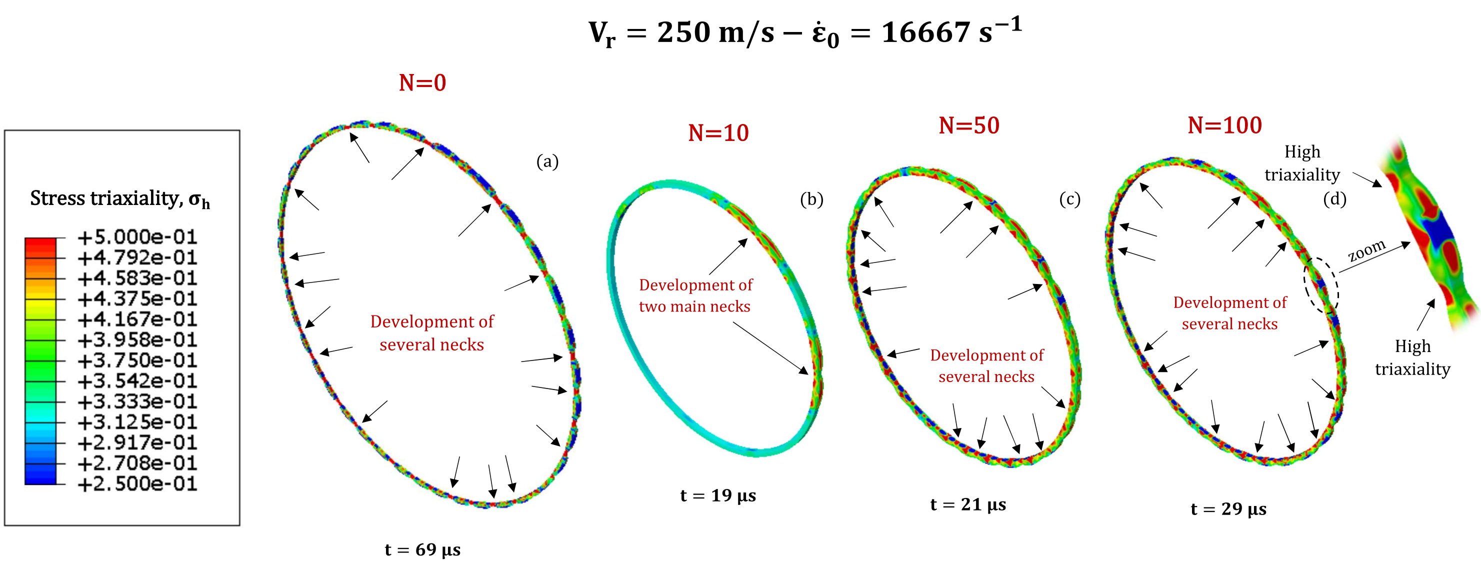

Figure 5: Contours of stress triaxiality σ_h. Imposed initial strain rate of $\dot{\varepsilon}_0 = 16667$ s^{-1} (which corresponds to $V_r = 250$ m/s). (a) Number of imperfections $N = 0$. Loading time $t = 69$ μs. (b) Number of imperfections $N = 10$. Loading time $t = 19$ μs. (c) Number of imperfections $N = 50$. Loading time $t = 21$ μs. (d) Number of imperfections $N = 100$. Loading time $t = 29$ μs. For $N = 10, 50$ and 100 the amplitude of the imperfections is $\Delta = 1\%$ and the random distribution of imperfection wavelengths is RDIW$_1$. All the isocontours have the same colour coding such that stress triaxialities ranging from 0.25 to 0.5 correlate with a colour scale that goes from blue to red. If the value of stress triaxiality is below 0.25, it remains blue, and if it is above 0.75, it remains red.

in the strain field that lead to the development of additional necks. The equivalent plastic strain contours of Fig. 7 illustrate the irregular distribution of the necks in the ring for both imperfection distributions. As in the case of RDIW_1 shown in Fig. 4(b), the average plastic strain outside the necks is ≈ 0.13 (this number can vary $\pm 15\%$ from *valley* to *valley*).

Fig. 6(b) displays the results for 50 geometric imperfections. The loading times for RDIW_2 and RDIW_3 are $t = 19$ μs and $t = 21$ μs, respectively, i.e. the time for the normalized equivalent plastic strain to reach 2.5 (slightly) depends on the imperfections distribution. Moreover, while the location of the necks is different for both imperfection distributions (as in the case of $N = 10$), the number of necks is very similar (13 for RDIW_2 and 14 for RDIW_3).

Fig. 6(c) shows the results for $N = 100$. As in the case of $N = 50$, the time required for RDIW_3 to reach the condition $\hat{\bar{\varepsilon}}^p = 2.5$ is slightly greater than for RDIW_2 (29 μs versus 27 μs). Moreover, the number of necks is similar for both imperfection distributions, 16 and 17 for RDIW_2 and RDIW_3, respectively. Similar number of necks was obtained for RDIW_1 with 100 imperfections (see Fig. 3(d)).

These results show that, although the number of necks depends on the number of imperfections, the number of necks is very similar for the different random distributions of imperfection wavelengths considered in this paper.

Fig. 8 shows the evolution of the number of necks formed in the ring n with the number of imperfections N for $\Delta = 1\%$ and $\dot{\varepsilon}_0 = 16667$ s^{-1}. The results obtained for five random distributions of imperfection wavelengths (RDIW_i with $i = 1, ..., 5$) are compared with the finite element calculations performed by Rodríguez-Martínez et al. [33] for rings with imperfections of the same amplitude ($\Delta = 1\%$) and constant wavelength (the N imperfections have the same wavelength).

The results of Rodríguez-Martínez et al. [33] show that for long and short wavelengths, $N \lesssim 6$ and $N \gtrsim 55$, inertia and stress multiaxiality, respectively, prevent the growth of the imperfections, giving rise to a dominant necking pattern formed by $n \approx 38$ necks which is hardly sensitive to the geometric perturbations (labeled as regions I and III in Fig. 2(a) of ref. [33]). Note that very similar number of necks is obtained for the calculation with $N = 0$ for which the necking pattern is triggered by the numerical perturbations introduced by the software. In contrast, for intermediate wavelengths $14 \lesssim N \lesssim 50$ each geometric perturbation leads to the nucleation of a single neck (region II of Fig. 2(a) in ref. [33]). For $14 \lesssim N \lesssim 50$, the wavelength of

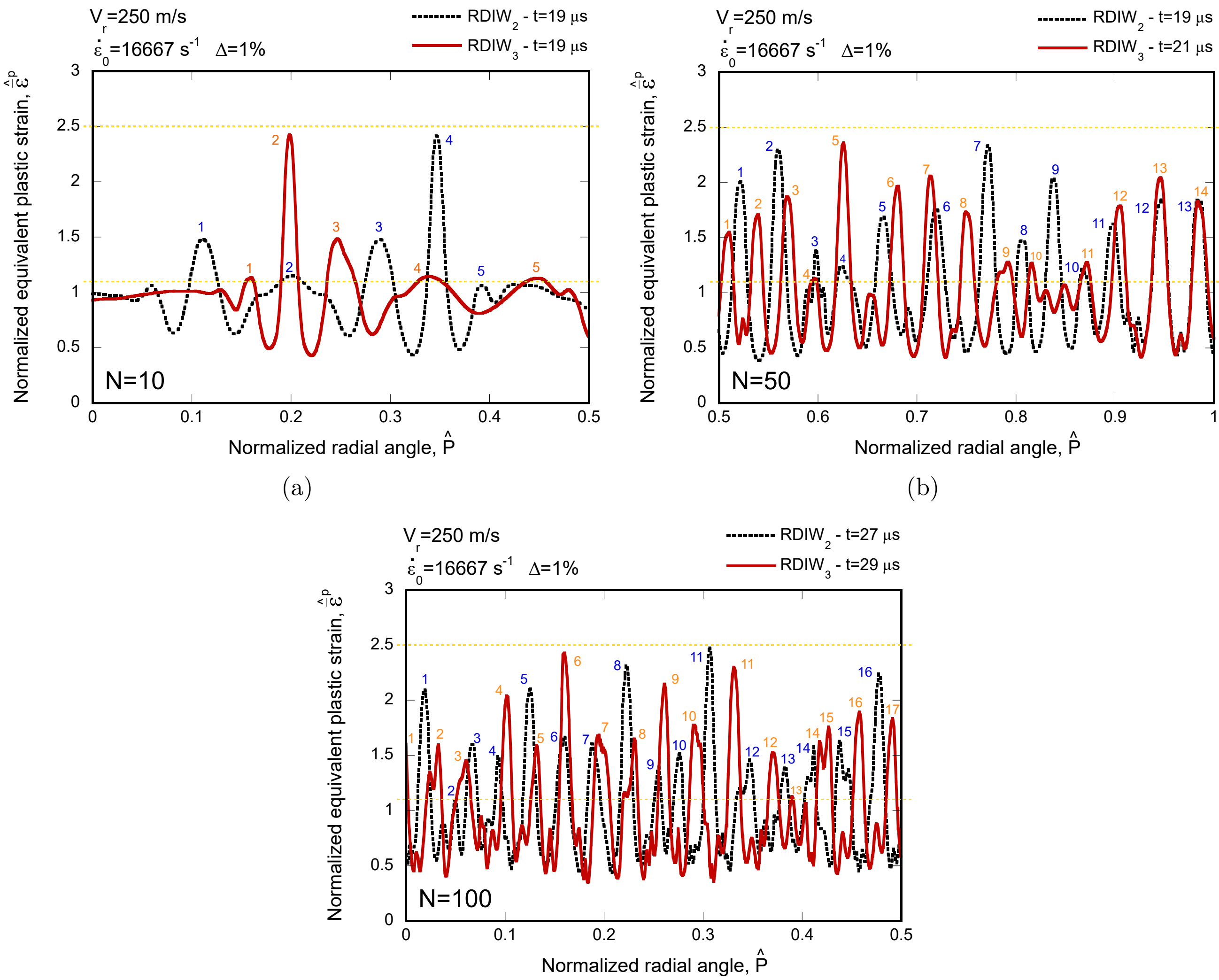

(a) (b) (c)

Figure 6: Normalized equivalent plastic strain $\hat{\bar{\varepsilon}}^p$ versus normalized outer perimeter of the ring $\hat{P}$. Imposed initial strain rate of $\dot{\varepsilon}_0 = 16667\ \mathrm{s}^{-1}$ (which corresponds to $V_r = 250$ m/s). Results are shown for two random distributions of imperfection wavelengths: RDIW_2 and RDIW_3. The amplitude of the imperfections is $\Delta = 1\%$. (a) Number of imperfections $N = 10$. The loading time for both RDIW_2 and RDIW_3 is $t = 19$ μs. (b) Number of imperfections $N = 50$. The loading times for RDIW_2 and RDIW_3 are $t = 19$ μs and $t = 21$ μs, respectively. (c) Number of imperfections $N = 100$. The loading times for RDIW_2 and RDIW_3 are $t = 27$ μs and $t = 29$ μs, respectively. The horizontal yellow dashed lines correspond to the conditions $\hat{\bar{\varepsilon}}^p = 1.1$ and $\hat{\bar{\varepsilon}}^p = 2.5$. For interpretation of the references to color in this figure, the reader is referred to the web version of this article.

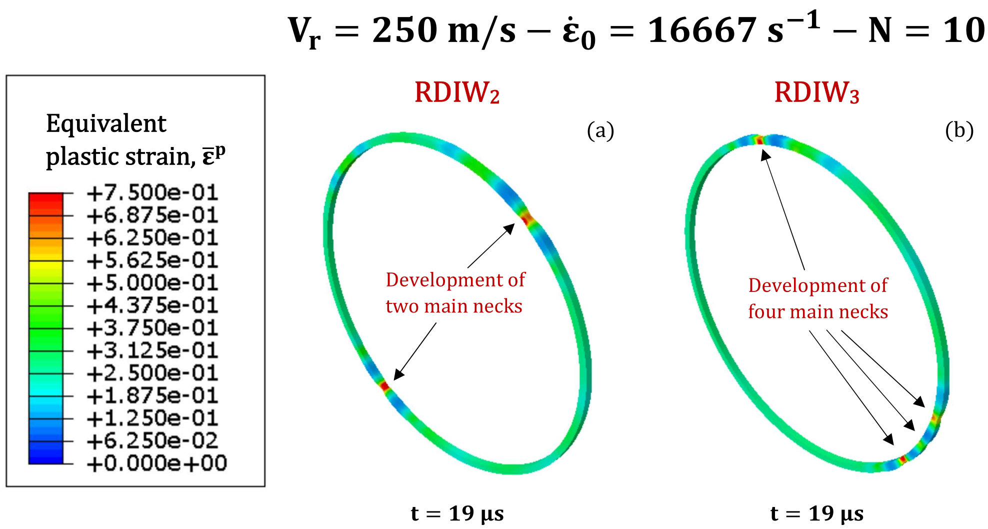

Figure 7: Contours of equivalent plastic strain $\bar{\varepsilon}^p$. Imposed initial strain rate of $\dot{\varepsilon}_0 = 16667$ s^{-1} (which corresponds to $V_r = 250$ m/s). Number of imperfections $N = 10$. The amplitude of the imperfections is $\Delta = 1\%$. Loading time $t = 19$ μs (a) Random distribution of imperfection wavelengths RDIW$_2$. (b) Random distribution of imperfection wavelengths RDIW$_3$.

the geometric imperfections is *close* to the critical neck size (i.e. the neck size for which the energy required to trigger the neck is minimum [45]), promoting early localization of plastic deformation at the locations of minimum thickness. To be noted that the unit-cell finite element calculations reported by Rodríguez-Martínez et al. [32] (Fig. 18) showed that the critical neck size for a circular bar with cross-section diameter 1 mm, imperfection amplitude 5% (area reduction), subjected to initial strain rate $\dot{\varepsilon}_0 = 15000$ s^{-1} and modeled with the same material behavior, is ≈ 2.2 mm. This critical neck size corresponds to the wavelength obtained for $N = 44$, which finds good agreement with the number of necks $n \approx 38$ which form the dominant necking pattern (i.e. the critical neck size seems to be directly connected to the number of necks in the dominant necking pattern).

The results obtained in this paper for random distributions of geometric perturbations show the effect of including imperfections with different wavelengths in the number of necks. In contrast to the results for constant wavelength imperfections [33], the number of necks n increases nonlinearly with N, displaying a concave-downward shape with decreasing slope as the number of imperfections increases. Note that, while the scatter in the results obtained for the 5 random distributions of imperfection wavelengths is generally small, it increases with N. The increasing scatter is partially attributed to the necking criterion that, for the largest values of N considered, identifies as necks some *non-localized* excursions of strain caused by the imperfections that have not been suppressed at the time the necking condition is met (see Fig. 12, Appendix B and ref. [33]). The problem is to determine a necking criterion that works well for small and large numbers of imperfections (and different loading rates and imperfection amplitudes, as will be shown in Figs. 9 and 12) since both the background strain when the necks are formed and the rate of growth of the necks depend on the number of imperfections (see Fig. 4). Nevertheless, as mentioned before, the trends and conclusions obtained in this paper do not seem to depend on the specific necking criterion considered. For a small number of imperfections there is a large variability in the distribution of the wavelengths of the geometric perturbations, see Fig. 2. For $N \lesssim 20$, the number of necks is similar to the number of imperfections (only for the distributions RDIW_1 and RDIW_4, and $N = 5$, the number of necks, $n = 16$, is significantly greater than the number of imperfections). The number of necks is controlled by the imperfections whose wavelength is closer to the critical neck size (which, as mentioned before, is ≈ 2.2 mm based on the results in ref. [32] for similar strain rate). These geometric perturbations grow faster and lead to disturbances in the strain field that, due to inertia effects, activate additional necking modes, see Figs. 3(b) and 6(a). Both the spacing and the growth rate of the necks are irregular, see also Figs. 3(b) and 6(a). As the number of imperfections increases, the variability in the distribution of the wavelengths of the geometric perturbations decreases, see Fig. 2. For $N > 20$, the number of necks is smaller than the number of imperfections. The geometric perturbations with shorter and longer wavelengths are suppressed by stress multiaxiality and inertia, respectively [33, 29, 49]. The resulting localization pattern is formed by an array of *more regularly* spaced necks with *more similar* growth rate, see Figs. 4(c)-(d) and 6(b)-(c). The locations of the necks only show partial correlation with the initial distribution of imperfections, and the correlation decreases as N increases, see also Figs. 4(c)-(d) and 6(b)-(c). Notice that for large N, the number of necks obtained in the calculations with imperfections of varying wavelength approaches the dominant necking pattern.

These results suggest that, if the variability in the distribution of the wavelengths of the geometric perturbations is large, the necking pattern is mostly controlled by the geometric perturbations. In contrast, as the variability decreases, the stabilizing effects of inertia and stress multiaxiality seem to become increasingly important. This is a main outcome of this paper that, to the authors' knowledge, has not been reported before.

Fig. 9 shows the evolution of the number of necks formed in the ring n as a function of the number of imperfections N for greater strain rates and the same imperfection amplitude $\Delta = 1\%$. Namely, calculations for $\dot{\varepsilon}_0 = 33333\ \text{s}^{-1}$ and $66667\ \text{s}^{-1}$, are shown in Figs. 9(a) and 9(b), respectively. As in Fig. 8, the results

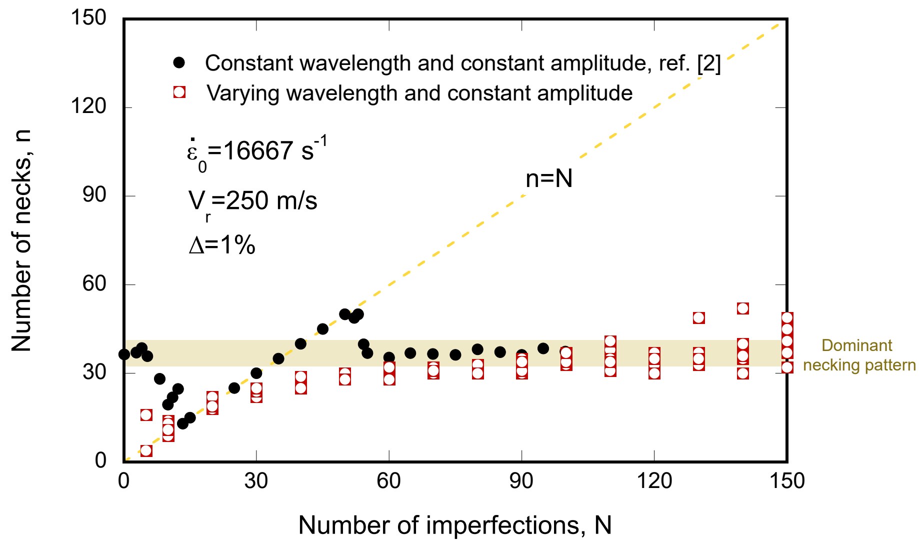

Figure 8: Number of necks n as a function of the number of imperfections N for an imposed initial strain rate of $\dot{\varepsilon}_0 = 16667$ s^{-1} (which corresponds to $V_r = 250$ m/s). The results obtained for five random distributions of imperfection wavelengths (RDIW$_i$ with $i = 1, ..., 5$) are compared with the finite element calculations performed by Rodríguez-Martínez et al. [33] for rings with constant wavelength imperfections. The amplitude of the imperfections is $\Delta = 1\%$.

obtained for five different distributions of imperfection wavelengths are compared with the calculations carried out by Rodríguez-Martínez et al. [33] for rings with constant wavelength imperfections. While the results display the same overall trends as for $\dot{\varepsilon}_0 = 16667$ s^{-1}, there are quantitative differences.

For instance, the calculations performed by Rodríguez-Martínez et al. [33] show that the number of necks corresponding to the dominant necking pattern increases from ≈ 38 for $\dot{\varepsilon}_0 = 16667$ s^{-1}, to ≈ 45 and ≈ 65 for $\dot{\varepsilon}_0 = 33333$ s^{-1} and 66667 s^{-1}, respectively. The increase in the number of necks is caused by inertia effects, which tend to decrease the critical neck size [32, 29]. Based on the finite element simulations shown in Fig. 18 of ref. [32], the critical neck sizes for imposed strain rates of 33333 s^{-1} and 66667 s^{-1} are ≈ 2 and ≈ 1.7, respectively. These critical neck sizes correspond to 49 and 57 imperfections, respectively, values which are close to the number of necks in the corresponding dominant necking patterns. In addition, the range of imperfections for which each geometric perturbation leads to the nucleation of a single neck enlarges with the strain rate, and extends from $N = 18$ to $N = 80$ for 33333 s^{-1}, and from $N = 25$ to $N = 120$ for 66667 s^{-1}, so that both lower and upper bound are shifted to larger values of N with the increase of $\dot{\varepsilon}_0$. These results indicate that increasing the strain rate enables the growth of smaller imperfections, which is consistent with the calculations of Rodríguez-Martínez et al. [32], who showed that increasing the strain rate leads to the increase of the strain for which the necks are formed (see also Fig. 11), which in turn leads to the reduction of the range of wavelengths suppressed by stress multiaxiality (see Fig. 12 in ref. [32]).

Accordingly, the results obtained in the present paper with random distributions of wavelengths show that, by increasing the strain rate, it is necessary to increase the number of imperfections so that the number of necks approaches the dominant necking pattern. Actually, for $\dot{\varepsilon}_0 = 66667$ s^{-1} the number of necks for the largest values of N considered is (generally) slightly below the dominant necking pattern. Note also that the scatter in the results obtained for large values of N increases with $\dot{\varepsilon}_0$, illustrating the difficulties to define a necking criterion that only captures actual necks (i.e. localized excursions of strain) for a wide range of loading rates and imperfection amplitudes.

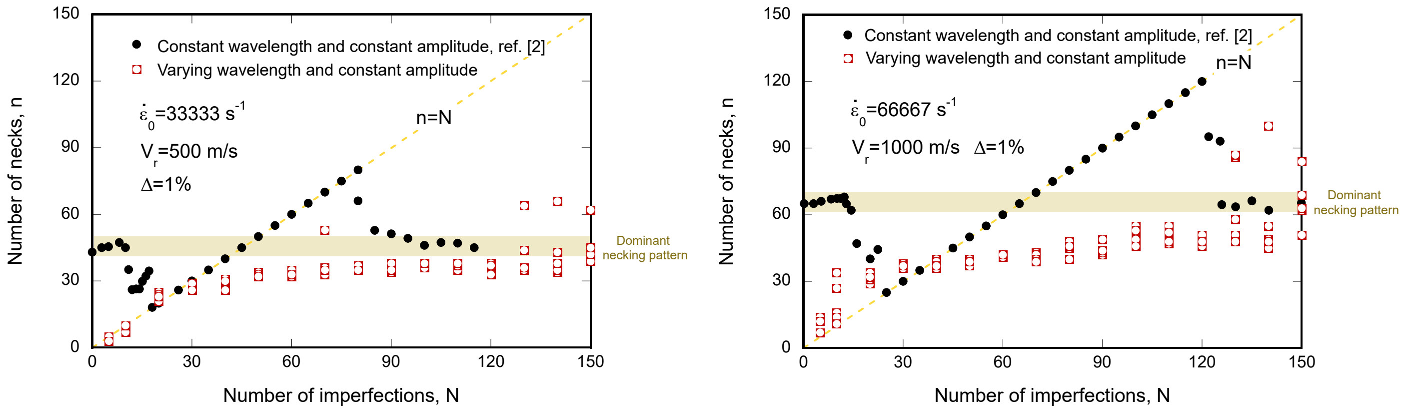

(a) (b)

Figure 9: Number of necks n as a function of the number of imperfections N. The results obtained for five random distributions of imperfection wavelengths (RDIW$_i$ with $i = 1, ..., 5$) are compared with the finite element calculations performed by Rodríguez-Martínez et al. [33] for rings with constant wavelength imperfections. The amplitude of the imperfections is $\Delta = 1\%$. (a) Imposed initial strain rate of $\dot{\varepsilon}_0 = 33333$ s^{-1} (which corresponds to $V_r = 500$ m/s) and (b) imposed initial strain rate of $\dot{\varepsilon}_0 = 66667$ s^{-1} (which corresponds to $V_r = 1000$ m/s).

The effect of the strain rate in the multiple necking pattern is further investigated in Fig. 10 which shows the normalized equivalent plastic strain $\hat{\bar{\varepsilon}}^p$ versus the normalized outer perimeter of the ring $\hat{P}$ for two imposed initial strain rates, $\dot{\varepsilon}_0 = 16667$ s^{-1} and $\dot{\varepsilon}_0 = 66667$ s^{-1}. The amplitude of the imperfections is $\Delta = 1\%$ and the random distribution of imperfection wavelengths is RDIW$_1$. The results correspond to the cases with $N = 10, 50, 100$ and 150. For these four cases, the increase of $\dot{\varepsilon}_0$ leads to an increase in the number of necks. It is clear from the results of Figs. 10(a)-(b) that the strain rate (due to inertia effects) activates necking modes of smaller size [32, 30]. The orange arrows included in these two graphs indicate the additional necks that are developed in the calculations corresponding to $\dot{\varepsilon}_0 = 66667$ s^{-1}. In Figs. 10(c)-(d), due to the large number of strain excursions, is more complicated to identify which additional necks are formed with the increase of the strain rate, and which ones are suppressed. On the other hand, the results in these two graphs show that, for large values of N, there are *non-localized* excursions of strain that meet the necking criterion (although they are not necks since the deformation is not localized), and contribute to the scatter in the results presented in Figs. 8 and 9. Some of these *non-localized* excursions of strain are indicated with green arrows.

Fig. 11 depicts contours of equivalent plastic strain for the calculations corresponding to $\dot{\varepsilon}_0 = 66667$ s^{-1} included in Fig. 10 and the same loading times. The comparison with the contours of Fig. 4 shows that the average equivalent plastic strain outside the necks increases with the strain rate (due to inertia effects which delay localization, e.g. see ref. [43]). For instance, for $N = 100$ and 16667 s^{-1} the average strain outside the necks is ≈ 0.18 (see discussion of Fig. 3(d)), and for the same number of imperfections and 66667 s^{-1} is approximately 0.53. As mentioned before, these differences in the average strain at which necks nucleate for different strain rates make more complicated to define a necking criterion that only captures *actual necks* for a wide range of loading rates. Moreover, the comparison of Figs. 11 and 4 also illustrates that the number of necks increases with the strain rate, especially when the number of imperfections is small.

The comparison between calculations with different imperfection amplitudes is performed in Fig. 12, which shows the normalized equivalent plastic strain $\hat{\bar{\varepsilon}}^p$ versus the normalized outer perimeter of the ring $\hat{P}$ for $\Delta = 1\%$ and 2.5%, and an imposed initial strain rate of 16667 s^{-1}. The random distribution of imperfection wavelengths is RDIW$_1$. Results are shown for calculations with $N = 10$, 50 and 100. The loading time for which the necking condition is met is smaller as the imperfection amplitude increases, i.e. the increase of the imperfection amplitude favors early necking formation. Moreover, the number of necks increases as the imperfections amplitude increases, notably for large number of imperfections. This is most likely because the increase of Δ decreases the stabilizing effect of stress multiaxiality on short wavelengths and enables the growth of additional smaller necks (see also Fig. 15 in ref. [32]). Some of these additional necks are indicated with orange arrows in Figs. 12(b) and 12(c). On the other hand, note that the increase of Δ also favors that the necking criterion is met by additional *non-localized* excursions of strain. Some of these *non-localized* strain peaks are indicated in Figs. 12(b) and 12(c) with green arrows. This shows that it is difficult to define a necking criterion which captures only *actual necks* for a wide range of imperfection amplitudes.

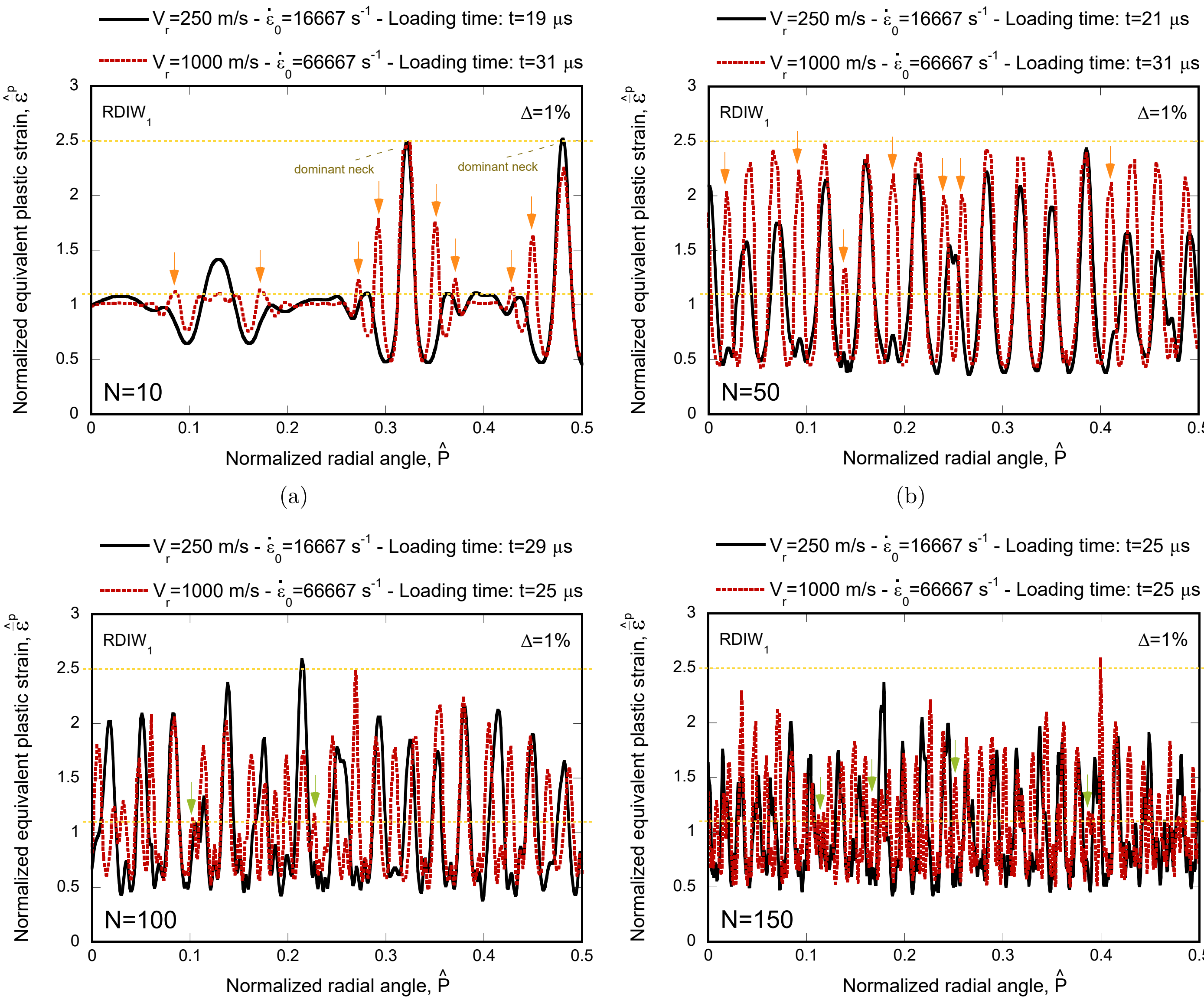

(a) (b) (c) (d)

Figure 10: Normalized equivalent plastic strain $\hat{\bar{\varepsilon}}^p$ versus normalized outer perimeter of the ring $\hat{P}$. The amplitude of the imperfections is $\Delta = 1\%$ and the random distribution of imperfection wavelengths is RDIW$_1$. Comparison between results obtained for two imposed initial strain rates, $\dot{\varepsilon}_0 = 16667$ s^{-1} and $\dot{\varepsilon}_0 = 66667$ s^{-1}, which correspond to $V_r = 250$ m/s and $V_r = 1000$ m/s, respectively. (a) Number of imperfections $N = 10$. The loading times for 16667 s^{-1} and 66667 s^{-1} are $t = 19$ μs and $t = 31$ μs, respectively. (b) Number of imperfections $N = 50$. The loading times for 16667 s^{-1} and 66667 s^{-1} are $t = 21$ μs and $t = 31$ μs, respectively. (c) Number of imperfections $N = 100$. The loading times for 16667 s^{-1} and 66667 s^{-1} are $t = 29$ μs and $t = 25$ μs, respectively. (d) Number of imperfections $N = 150$. The loading time for both 16667 s^{-1} and 66667 s^{-1} is $t = 25$ μs. The horizontal yellow dashed lines correspond to the conditions $\hat{\bar{\varepsilon}}^p = 1.1$ and $\hat{\bar{\varepsilon}}^p = 2.5$. For interpretation of the references to color in this figure, the reader is referred to the web version of this article.

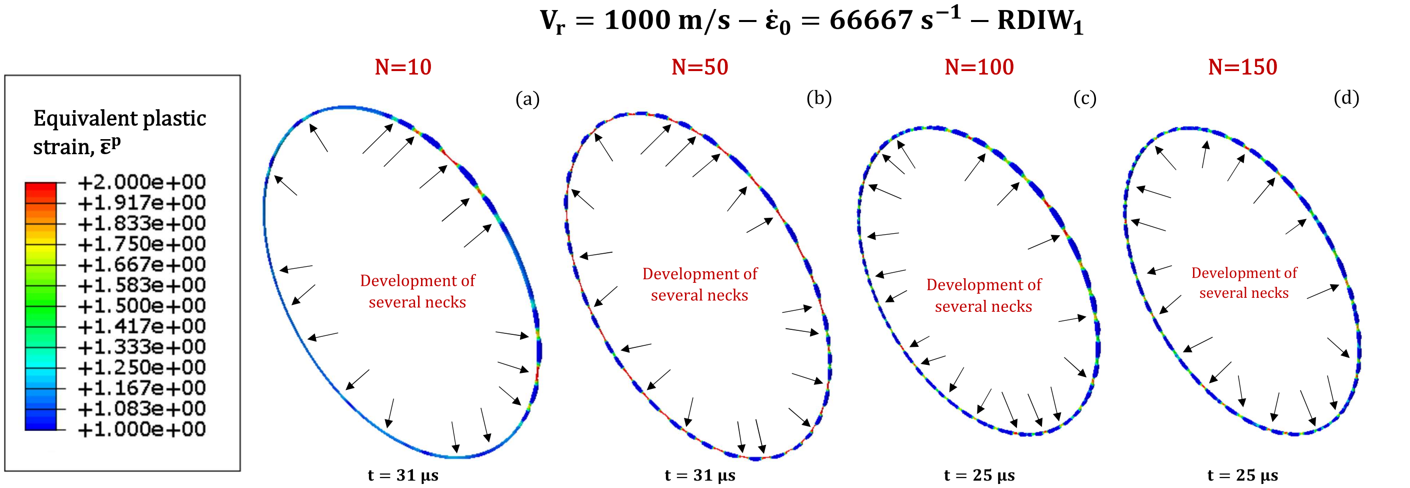

Figure 11: Contours of equivalent plastic strain $\bar{\varepsilon}^p$. Imposed initial strain rate of $\dot{\varepsilon}_0 = 66667$ s^{-1} (which corresponds to $V_r = 1000$ m/s). (a) Number of imperfections $N = 10$. Loading time $t = 31$ μs. (b) Number of imperfections $N = 50$. Loading time $t = 31$ μs. (c) Number of imperfections $N = 100$. Loading time $t = 25$ μs. (d) Number of imperfections $N = 150$. Loading time $t = 25$ μs. The amplitude of the imperfections is $\Delta = 1\%$ and the random distribution of imperfection wavelengths is RDIW$_1$.

3.2. Varying amplitude imperfections

Fig. 13 shows the evolution of the number of necks formed in the ring n with the number of imperfections N for $\dot{\varepsilon}_0 = 33333$ s^{-1}. The results obtained for five random distributions of wavelengths (RDIW$_i$ with $i = 1, ..., 5$) with imperfections of constant and varying amplitude are compared with the finite element calculations performed by Rodríguez-Martínez et al. [33] for rings with imperfections of constant wavelength and amplitude (i.e. the black and red markers correspond to results already shown in Fig. 9(a)). For the constant amplitude imperfections $\Delta = 1\%$. For the varying amplitude imperfections, the random distribution of imperfection amplitudes is bounded between 0.5% and 1.5%, with the mean of the distribution being $\Delta_{\text{avg}} = 1\%$. The results obtained with random distributions of wavelengths of constant and varying amplitude are generally similar. The variation in the imperfections amplitude considered does not have a great impact in the number of necks, e.g. notice that the number of necks for large values of N is also close to the dominant pattern. However, for some of the calculations with smaller number of imperfections, the simulations with imperfections of varying amplitude predict greater number of necks (indicated with orange arrows). These are generally calculations for which small amplitude imperfections (smaller than the average) lead to the development of additional necks.

A comparison between the necking patterns obtained with imperfections of constant and varying amplitude is performed below. Fig. 14 shows the normalized equivalent plastic strain $\hat{\bar{\varepsilon}}^p$ versus the normalized outer

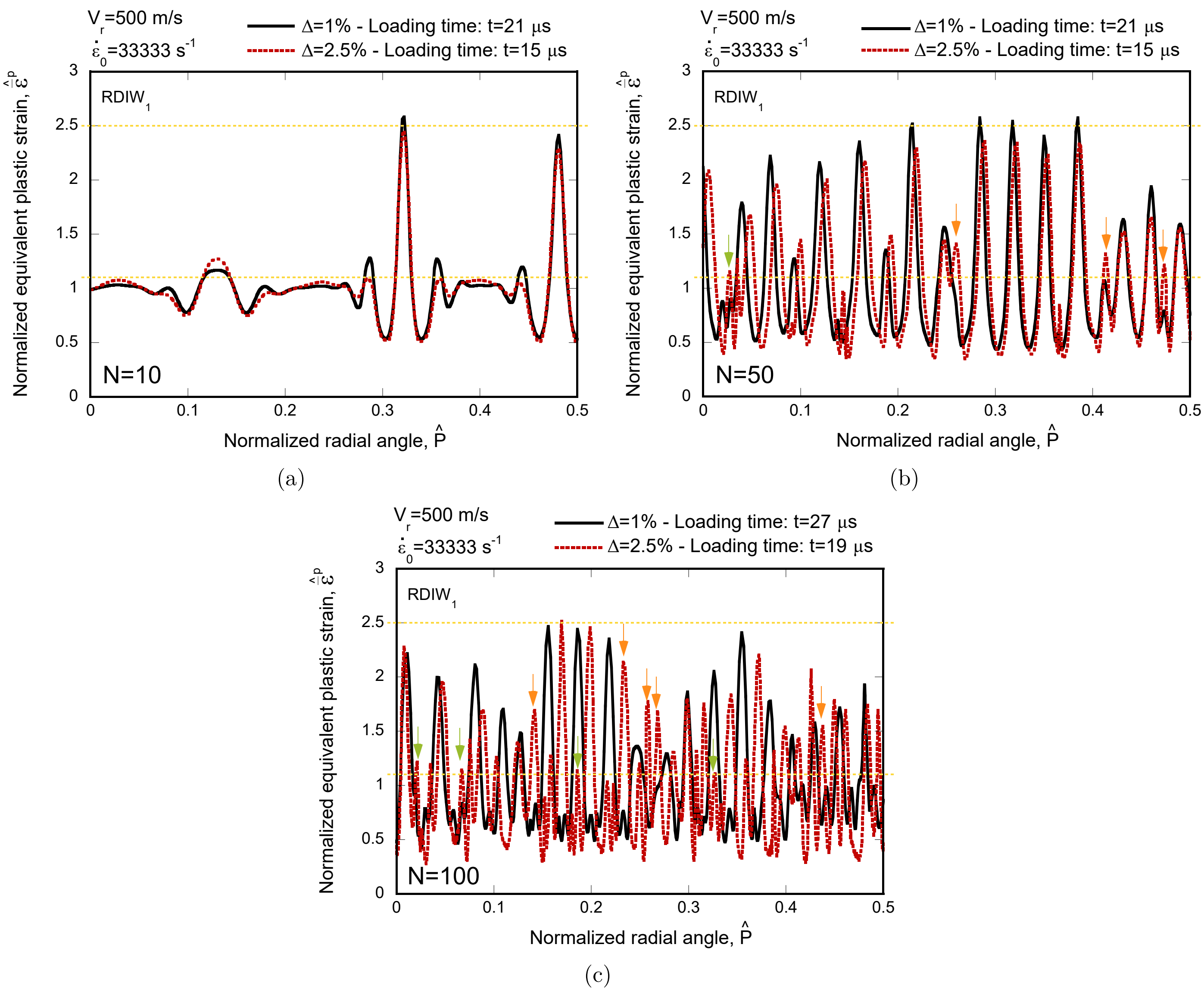

Figure 12: Normalized equivalent plastic strain $\hat{\bar{\varepsilon}}^p$ versus normalized outer perimeter of the ring $\hat{P}$. The imposed initial strain rate is $\dot{\varepsilon}_0 = 16667 \text{ s}^{-1}$ (which corresponds to $V_r = 250$ m/s). Comparison between results obtained for two imperfection amplitudes: $\Delta = 1\%$ and $\Delta = 2.5\%$. The random distribution of imperfection wavelengths is RDIW$_1$. (a) Number of imperfections $N = 10$. The loading times for $\Delta = 1\%$ and $\Delta = 2.5\%$ are $t = 21$ μs and $t = 15$ μs, respectively. (b) Number of imperfections $N = 50$. The loading times for $\Delta = 1\%$ and $\Delta = 2.5\%$ are $t = 21$ μs and $t = 15$ μs, respectively. (c) Number of imperfections $N = 10$. The loading times for $\Delta = 1\%$ and $\Delta = 2.5\%$ are $t = 27$ μs and $t = 19$ μs, respectively. The horizontal yellow dashed lines correspond to the conditions $\hat{\bar{\varepsilon}}^p = 1.1$ and $\hat{\bar{\varepsilon}}^p = 2.5$. For interpretation of the references to color in this figure, the reader is referred to the web version of this article.

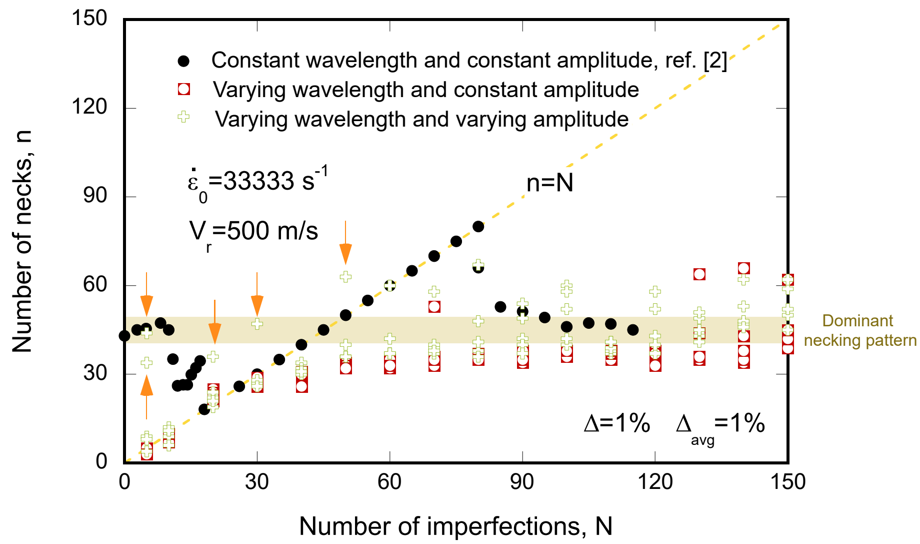

Figure 13: Number of necks n as a function of the number of imperfections N for an imposed initial strain rate of $\dot{\varepsilon}_0 = 33333\ \mathrm{s}^{-1}$ (which corresponds to $V_r = 500$ m/s). The results obtained for five random distributions of wavelengths (RDIW$_i$ with $i = 1, ..., 5$) with imperfections of constant and varying amplitude are compared with the finite element calculations performed by Rodríguez-Martínez et al. [33] for rings with imperfections of constant wavelength and amplitude (i.e. the black and red markers correspond to results already shown in Fig. 9(a)). For the constant amplitude imperfections $\Delta = 1\%$. For the varying amplitude imperfections, the random distribution of imperfection amplitudes is bounded between 0.5% and 1.5%, with the mean of the distribution being $\Delta_{\mathrm{avg}} = 1\%$. For interpretation of the references to color in this figure, the reader is referred to the web version of this article.

perimeter of the ring $\hat{P}$ for an imposed initial strain rate of $\dot{\varepsilon}_0 = 33333\ \mathrm{s}^{-1}$. The random distribution of imperfection wavelengths is RDIW$_2$. For the constant amplitude imperfections $\Delta = 1\%$. For the varying amplitude imperfections, the bounds and the mean of the amplitudes distribution are the same as in Fig. 13. Results are shown for $N = 10$, 50 and 100. Notice that the necking criterion is met (generally) earlier for the calculations with imperfections of varying Δ, most likely due to the faster growth of some of the geometric perturbations of greater amplitude. Moreover, the variation in the amplitudes distribution changes the location and growth rate of the necks with respect to the simulations with constant Δ, notably for the calculations with small number of imperfections, see the results in Fig. 14(a) for $N = 10$. If N is small, the necking pattern is controlled, to a large extent, by the imperfections with closer wavelengths to the critical neck size (see discussion of Fig. 8) and greater amplitude. As N increases, the influence of the distribution of amplitudes in the location and growth rate of the necks seems to be reduced, see the results in Figs. 14(b) and 14(c) for $N = 50$ and $N = 100$, respectively.

Fig. 15 shows the evolution of the average neck spacing L with the imposed initial strain rate $\dot{\varepsilon}_0$, where L has been calculated as the ratio between the initial outer perimeter of the ring and the number of necks. We

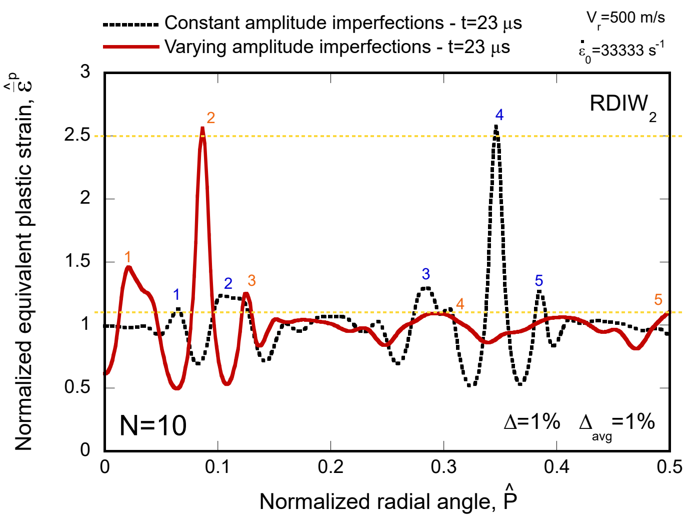

(a)

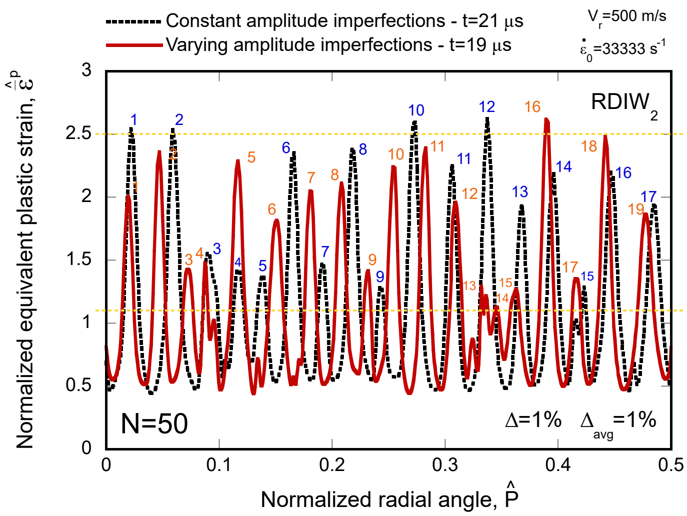

(b)

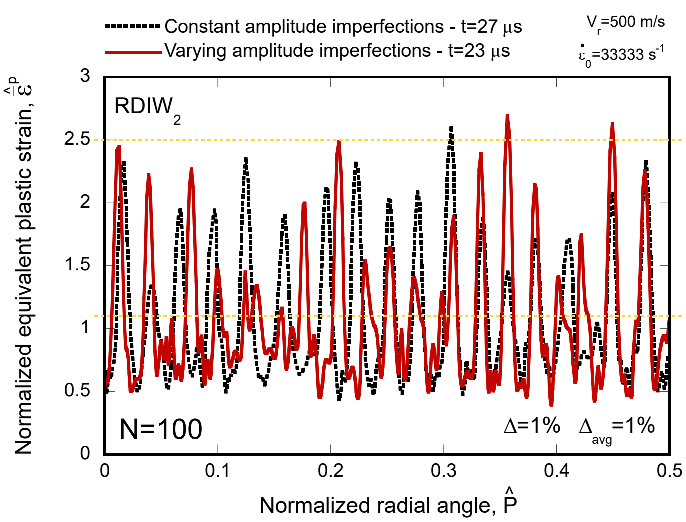

(c)

Figure 14: Normalized equivalent plastic strain $\hat{\bar{\varepsilon}}^p$ versus normalized outer perimeter of the ring $\hat{P}$. The imposed initial strain rate is $\dot{\varepsilon}_0 = 33333$ s^{-1} (which corresponds to $V_r = 500$ m/s). The random distribution of imperfection wavelengths is RDIW$_2$. Comparison between the results obtained with imperfections of constant and varying amplitude. For the constant amplitude imperfections $\Delta = 1\%$. For the varying amplitude imperfections, the random distribution of imperfection amplitudes is bounded between 0.5% and 1.5%, with the mean of the distribution being $\Delta_{\text{avg}} = 1\%$. (a) Number of imperfections $N = 10$. The loading time for the calculations with imperfections of constant and varying amplitude is $t = 23$ μs. (b) Number of imperfections $N = 50$. The loading times for the calculations with imperfections of constant and varying amplitude are $t = 21$ μs and $t = 19$ μs, respectively. (c) Number of imperfections $N = 100$. The loading times for the calculations with imperfections of constant and varying amplitude are $t = 27$ μs and $t = 23$ μs, respectively. The horizontal yellow dashed lines correspond to the conditions $\hat{\bar{\varepsilon}}^p = 1.1$ and $\hat{\bar{\varepsilon}}^p = 2.5$. For interpretation of the references to color in this figure, the reader is referred to the web version of this article.

show finite element results corresponding to imperfections of varying wavelength and amplitude for $N = 10$, 50 and 100 (black markers in Figs. 15(a)-(b)-(c)). Recall from Section 2 that the average imperfection wavelengths corresponding to $N = 10$, 50 and 100 are $\lambda_{\text{avg}} \approx 10$ mm, 2 mm and 1 mm, respectively. The distribution of imperfection wavelengths is RDIW_1, and the imperfection amplitudes range between 0.5% and 1.5%, with the mean of the distribution being $\Delta_{\text{avg}} = 1\%$, as in Figs. 13 and 14. For $N = 10$, the evolution of L with the strain rate is irregular and does not display any specific trend. The values of the average neck spacing are relatively close to the average imperfection wavelength $\lambda_{\text{avg}} \approx 10$ (indicated with a yellow dashed line). As in the case of the distributions of imperfections with constant amplitude (Section 3.1), if the variability in the wavelength of the imperfections is large (i.e. if N is small), the necking pattern is generally controlled by the geometric perturbations. In contrast, for $N = 50$ the value of L displays a monotonic decrease with the strain rate, with a rate of decrease which is smaller as $\dot{\varepsilon}_0$ increases. As mentioned in Section 3, the decrease in L is caused by inertia, which activates smaller neck sizes with the increase of the strain rate [32]. Moreover, the average neck spacing is greater than the corresponding average imperfection wavelength, which reveals than the number of necks is smaller than the number of imperfections for the whole range of strain rates investigated. As mentioned in Section 3.1, for large N, the smaller imperfection wavelengths are suppressed by the stress multiaxiality effects [33]. For $N = 100$, the evolution of L with the strain rate is qualitatively the same as in the case of $N = 50$. The difference is that the values of L are smaller for $N = 100$ for all the strain rates considered. Nevertheless, notice that the increasing role played by inertia in the necking pattern as the strain rates increases [32] tends to reduce the gap in the values of L obtained for $N = 50$ and 100.

Fig. 15(a) shows a comparison of the finite element results corresponding to imperfections of varying wavelength and amplitude (black markers) with the finite element calculations without imperfections ($N = 0$) performed by Rodríguez-Martínez et al. [33] (green markers) and the linear stability analysis predictions reported by N'souglo et al. [30] (red line). The results of Rodríguez-Martínez et al. [33] for $N = 0$, which are obtained with the same material modeling used in this paper (as mentioned before), show a decrease of L with the strain rate, in qualitative agreement with the calculations for $N = 50$ and $N = 100$. On the other hand, note that, while at low strain rates the calculations of Rodríguez-Martínez et al. [33] find closer quantitative agreement with the average neck spacing obtained for $N = 50$, at high strain rates the results of Rodríguez-Martínez et al. [33] lay in between the calculations performed for $N = 50$ and 100. As inertia becomes more important, the geometric imperfections seem to play a smaller role in the average neck spacing such that if the variability in the distribution of imperfections wavelengths is not large (i.e. if N is large), the results are similar to the calculations without imperfections. On the other hand, the linear stability analysis predictions of N'souglo et al. [30], that were obtained for bars with circular cross section, subjected to dynamic stretching, and modeled with Gurson plasticity, show a gradual decrease of L with the strain rate. Despite the different material behaviors considered in the finite element calculations and the stability analysis, the analytical and numerical results show good qualitative and quantitative agreement, especially at high strain rates, for which the average neck spacing obtained with the analytical model lays between the simulations corresponding to $N = 50$ and 100, and virtually overlaps with the calculations performed by Rodríguez-Martínez et al. [33]. In other words, provided that inertia effects are important, the linear stability analysis yields good predictions for the average neck spacing for specimens with and without distributions of geometric imperfections (even if the material behavior is different [32, 30]).

Figs. 15(b)-(c) present a comparison of the finite element results corresponding to imperfections of varying wavelength and amplitude (black markers) with the experiments performed by Grady and Benson [9] with Aluminium 1100-O and OFHC copper rings (green markers), and with the simulations conducted by Guduru and Freund [12] with circular cross-section bars modeled with Gurson plasticity, without geometric imperfections, and subjected to dynamic stretching (red markers). Despite the differences in the constitutive framework used to describe the material behavior, the calculations of Guduru and Freund [12] find good qualitative agreement with the simulations performed for $N = 50$ and 100 (material properties values in this paper and in the simulations of Guduru and Freund [12] are different, check Section 5 in Guduru and Freund [12] for the specific parameters values they used). As the calculations of Rodríguez-Martínez et al. [33] for $N = 0$ (see Fig. 15(a)), with the increase of the strain rate, the simulations of Guduru and Freund [12] for both Aluminium 1100-O and OFHC copper specimens deviate from the data obtained for $N = 50$ and approach the results for $N = 100$. Moreover, despite the limited range of strain rates explored in the tests of Grady and Benson [9], the experimental data display a decrease in the average neck spacing that shows qualitative agreement with the finite element calculations performed with imperfections of varying wavelength and amplitude, and also with the calculations of Guduru and Freund [12]. Notice that the decrease of the average necks spacing with the strain rate, displaying a concave-upwards shape, has been observed in computations performed with several ductile materials, with very different mechanical behaviors

[12, 32, 43, 30, 29] (i.e. the qualitative agreement between experiments and simulations is obtained for almost any metallic material provided that it is ductile and inertia effects are important). Moreover, the quantitative differences between the experiments and the simulations are likely due to the fact the constitutive models used in the simulations were not calibrated to describe the mechanical response of the materials used in the tests. Nevertheless, this conclusion needs further research.

4. Concluding remarks

This paper provides a comprehensive finite element investigation on the effect of geometric imperfections in the formation of multiple necks in ductile rings subjected to rapid radial expansion. We have extended previous works of Han and Tvergaard [13], Sørensen and Freund [36], Guduru and Freund [12] and Rodríguez-Martínez et al. [33] by considering rings with random distributions of geometric imperfections of varying amplitude and wavelength. The calculations show that the effect of geometric perturbations on the number and grow rate of the necks depends on the variability in the wavelength and amplitude of the imperfections. Namely, if the variability is large, the effect of geometric imperfections in the necking pattern is large. In contrast, if the variability in wavelengths and amplitudes distribution is small, the stabilizing effects of inertia and stress multiaxiality become more important, and the number of necks approaches the dominant necking pattern obtained in finite element simulations with no *ab initio* geometric imperfections. Moreover, the variation in the imperfections amplitude considered in this paper does not have a great impact in the number of necks. This investigation should be continued further by using constitutive models representative of actual materials (e.g. accounting for strain hardening, strain rate sensitivity and thermal softening), and performing experiments with specimens with controlled surface roughness and geometric imperfections, in order to validate the main outcomes presented in this paper. Moreover, the effect of the geometric imperfections in the distribution of fragments sizes is a key issue that still needs further research efforts.

Acknowledgements

The research leading to these results has received funding from the European Research Council (ERC) under the European Union's Horizon 2020 research and innovation programme. Project PURPOSE, grant agreement 758056.

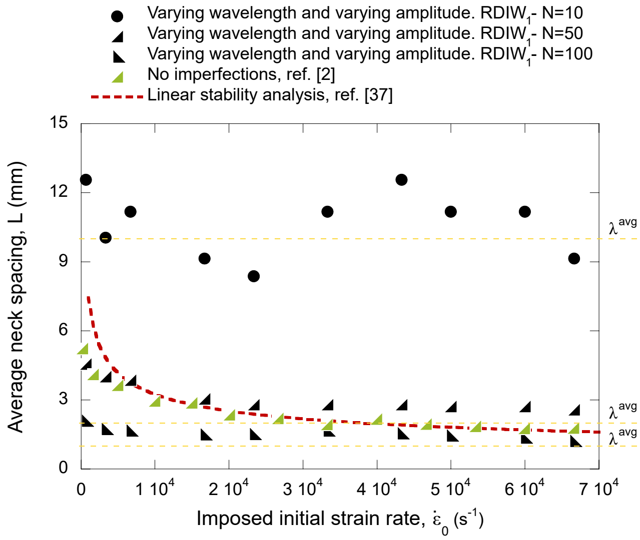

(a)

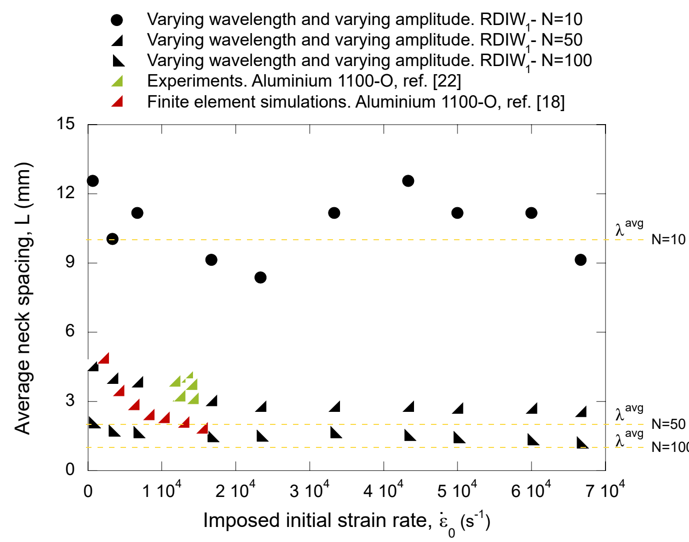

(b)

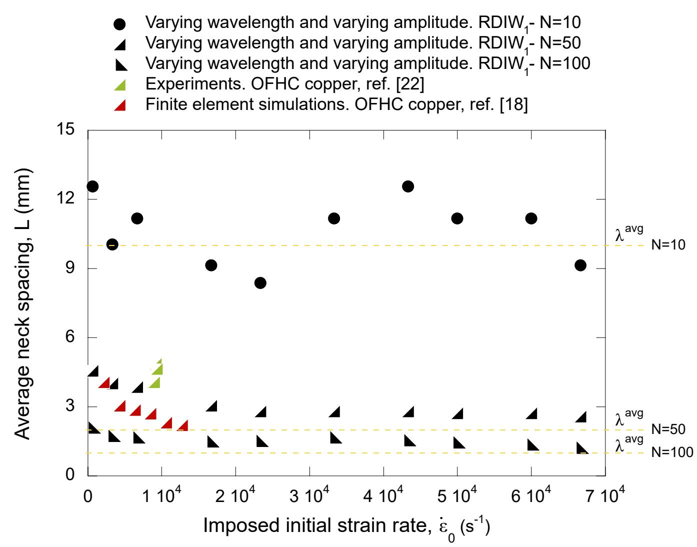

(c)

Figure 15: Average neck spacing L versus imposed initial strain rate $\dot{\varepsilon}_0$. Finite element results corresponding to imperfections of varying wavelength and amplitude for $N = 10$, 50 and 100. The random distribution of imperfection wavelengths is RDIW_1. The random distribution of imperfection amplitudes is bounded between 0.5% and 1.5%, with the mean of the distribution being $\Delta_{\mathrm{avg}} = 1\%$. (a) Comparison with the finite element results for $N = 0$ reported by Rodríguez-Martínez et al. [33] and the linear stability analysis predictions reported by N'souglo et al. [30]. (b) Comparison with the experiments performed by Grady and Benson [9] and the finite element results reported by Guduru and Freund [12] for Aluminium 1100-O specimens. (c) Comparison with the experiments performed by Grady and Benson [9] and the finite element results reported by Guduru and Freund [12] for OFHC copper specimens. The horizontal yellow dashed lines correspond to the average imperfection wavelengths for $N = 10$, 50 and 100. For interpretation of the references to color in this figure, the reader is referred to the web version of this article.

J.A.R.-M expresses sincere gratitude to Dr. Alain Molinari and Dr. Sébastien Mercier (University of Lorraine, Metz) for helpful discussions on multiple necking problems.

Appendix A. Mesh sensitivity analysis

Fig. A.16 shows the number of necks n as a function of the number of imperfections N for an imposed initial strain rate of $\dot{\varepsilon}_0 = 16667\ \mathrm{s}^{-1}$ (which corresponds to $V_r = 250$ m/s). The results are obtained for three different meshes: Mesh 1 with ≈ 100000 elements (the mesh used in the calculations presented in Section 3), Mesh 2 with ≈ 150000 elements and Mesh 3 with ≈ 200000 elements (i.e. the number of elements through the thickness of the ring is increased from 10, to 15 and 20). Recall from Section 2 that we have used variable element size, with the smaller elements being of the order of microns, in order to include several of them in the shorter imperfections wavelengths considered (e.g. for Mesh 3 the minimum element size is approximately $10\ \mu\mathrm{m} \times 10\ \mu\mathrm{m} \times 10\ \mu\mathrm{m}$). The results for Mesh 1 are obtained for five random distributions of imperfection wavelengths (RDIW$_i$ with $i = 1, ..., 5$), and the results for Mesh 2 and Mesh 3 are obtained with an additional random distribution of imperfection wavelengths RDIW$_6$. A comparison is performed with the finite element calculations carried out by Rodríguez-Martínez et al. [33] for rings with constant wavelength imperfections. The amplitude of the imperfections is $\Delta = 1\%$. The three different meshes yield the same qualitative results, with slight quantitative differences when the number of initial geometric imperfections is large. These differences are most likely due to the necking criterion and the identification as necks of some *non-localized* excursions of strain, see Section 3 and Appendix B. Nevertheless, these results show that the finite element mesh does not affect the general trends and conclusions obtained in this paper.

Appendix B. The influence of necking criterion

Fig. B.17 shows the number of necks n as a function of the number of imperfections N for an imposed initial strain rate of $\dot{\varepsilon}_0 = 16667\ \mathrm{s}^{-1}$. The results obtained for five random distributions of imperfection wavelengths (RDIW$_i$ with $i = 1, ..., 5$) are compared with the finite element calculations performed by Rodríguez-Martínez et al. [33] for rings with constant wavelength imperfections. The amplitude of the imperfections is $\Delta = 1\%$.

In Fig. B.17(a), the results corresponding to the random distributions of imperfection wavelengths are obtained using three different criteria. Criterion 1 (red markers) is the one that has been used in Section

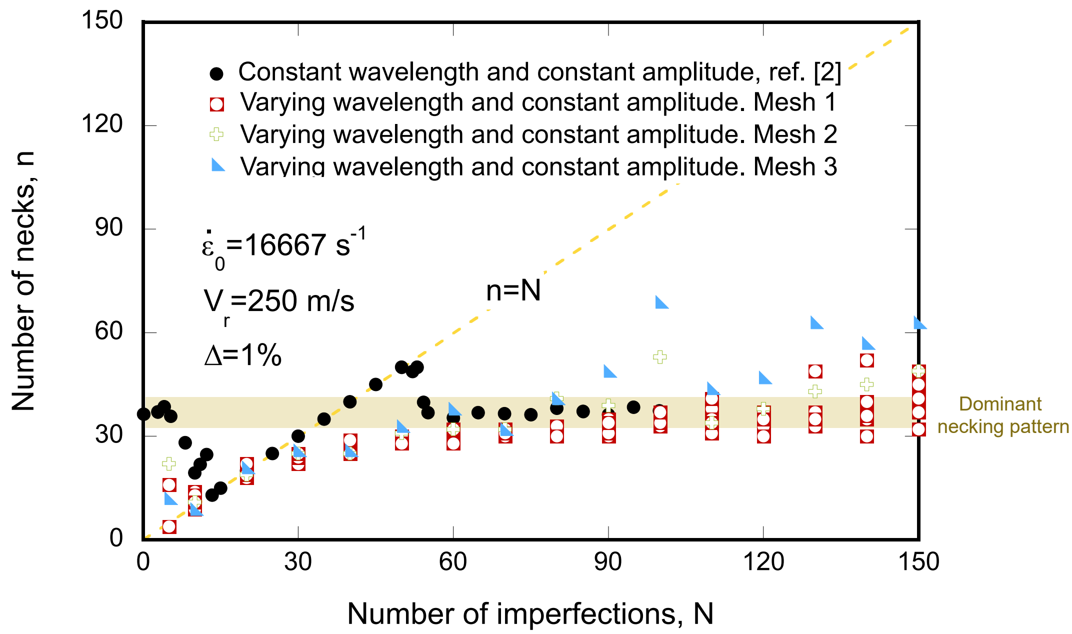

Figure A.16: Number of necks n as a function of the number of imperfections N for an imposed initial strain rate of $\dot{\varepsilon}_0 = 16667\ \mathrm{s}^{-1}$ (which corresponds to $V_r = 250$ m/s). The results are obtained for three different meshes: Mesh 1 with ≈ 100000 elements, Mesh 2 with ≈ 150000 elements and Mesh 3 with ≈ 200000 elements. The results for Mesh 1 are obtained for five random distributions of imperfection wavelengths (RDIW$_i$ with $i = 1, ..., 5$), and the results for Mesh 2 and Mesh 3 are obtained with an additional random distribution of imperfection wavelengths RDIW$_6$. A comparison is performed with the finite element calculations performed by Rodríguez-Martínez et al. [33] for rings with constant wavelength imperfections. The amplitude of the imperfections is $\Delta = 1\%$.

3 (these results were shown in Fig. 8), i.e. the necks are considered the excursions of strain that fulfill the condition $\hat{\bar{\varepsilon}}^p = 1.1$ when the maximum value of $\hat{\bar{\varepsilon}}^p$ reaches ≈ 2.5. For criteria 2 (green markers) and 3 (blue markers), the necking conditions are that the excursions of strain must reach $\hat{\bar{\varepsilon}}^p = 1.2$ and $\hat{\bar{\varepsilon}}^p = 1.3$, respectively, at the time that the maximum value of $\hat{\bar{\varepsilon}}^p$ is ≈ 2.5. Notice that the results obtained with the three criteria are very similar. The differences are only noticeable when the number of imperfections is small, such that the number of necks obtained with criterion 3 is slightly smaller than with criteria 1 and 2.

In Fig. B.17(b), the results corresponding to the random distributions of imperfection wavelengths are obtained with criteria 1 and 4. For the latter criterion, the necks are considered the excursions of strain that fulfill the condition $\hat{\bar{\varepsilon}}^p = 1.1$ at the time that the maximum value of $\hat{\bar{\varepsilon}}^p$ reaches ≈ 3. There are no significant differences between results obtained with criteria 1 and 4. As mentioned in Section 3, the scatter in the results for large values of N is related to the difficulty of defining criteria that only capture *actual necks* for a wide span of *ab initio* imperfections.

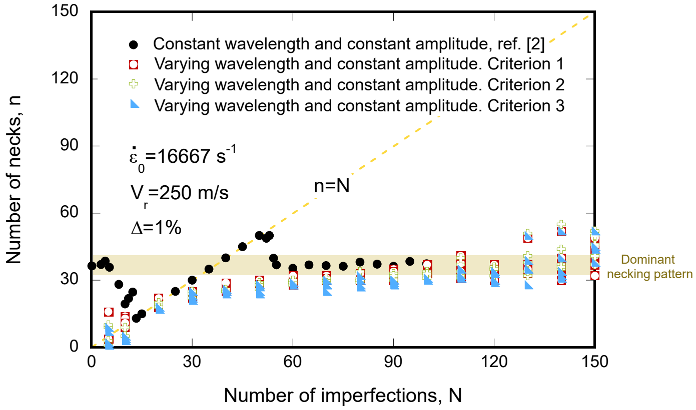

(a) (b)

Figure B.17: Number of necks n as a function of the number of imperfections N for an imposed initial strain rate of $\dot{\varepsilon}_0 = 16667\ \mathrm{s}^{-1}$ (which corresponds to $V_r = 250$ m/s). The results obtained for five random distributions of imperfection wavelengths (RDIW$_i$ with $i = 1, ..., 5$) are compared with the finite element calculations performed by Rodríguez-Martínez et al. [33] for rings with constant wavelength imperfections. The amplitude of the imperfections is $\Delta = 1\%$. The results corresponding to the random distributions of imperfection wavelengths are obtained using: (a) criteria 1, 2 and 3, (b) criteria 1 and 4. For interpretation of the references to color in this figure, the reader is referred to the web version of this article.

References

[1] ABAQUS/Explicit, 2016. Abaqus Explicit v6.16 User's Manual. Version 6.16 ed., ABAQUS Inc., Richmond, USA.

[2] Altynova, M., Hu, X., Daehn, G.S., 1996. Increased ductility in high velocity electromagnetic ring expansion. Metallurgical and Materials Transactions A 27, 1837–1844.

[3] Cliche, N., Ravi-Chandar, K., 2018. Dynamic strain localization in magnesium alloy AZ31B-O. Mechanics of Materials 116, 189 – 201. IUTAM Symposium on Dynamic Instabilities in Solids.

[4] El Maï, S., Mercier, S., Petit, J., Molinari, A., 2014. An extension of the linear stability analysis for the prediction of multiple necking during dynamic extension of round bar. International Journal of Solids and Structures 51, 3491–3507.

[5] Fressengeas, C., Molinari, A., 1985. Inertia and thermal effects on the localization of plastic flow. Acta Metallurgica 33, 387–396.

[6] Fressengeas, C., Molinari, A., 1994. Fragmentation of rapidly stretching sheets. European Journal of Mechanics A/Solids 13, 251–268.

[7] Goto, D., Becker, R., Orzechowski, T., Springer, H., Sunwoo, A., Syn, C., 2008. Investigation of the fracture and fragmentation of explosively driven rings and cylinders. International Journal of Impact Engineering 35, 1547–1556.

[8] Grady, D.E., 2002. Fragmentation of expanding cylinders and the statistical theory of N. F. Mott, in: Furnish, M.D., Thadhani, N.N., Horie, Y. (Eds.), Shock Compression of Condensed Matter - 2001), American Institute of Physics. pp. 799–802.

[9] Grady, D.E., Benson, D.A., 1983. Fragmentation of metal rings by electromagnetic loading. Experimental Mechanics 12, 393–400.

[10] Grady, D.E., Kipp, M.E., Benson, D.A., 1984. Energy and statistical effects in the dynamic fragmentation of metal rings, in: Harding, J. (Ed.), Mechanical properties at high strain rates, Institute of Physics, Bristol. pp. 315–320.

[11] Grady, D.E., Olsen, M.L., 2003. A statistics and energy based theory of dynamic fragmentation. International Journal of Impact Engineering 29, 293–306.

[12] Guduru, P.R., Freund, L.B., 2002. The dynamics of multiple neck formation and fragmentation in high rate extension of ductile materials. International Journal of Solids and Structures 39, 5615–5632.

[13] Han, J.B., Tvergaard, V., 1995. Effect of inertia on the necking behaviour of ring specimens under rapid axial expansion. European Journal of Mechanics A/Solids 14, 287–307.

[14] Hiroe, T., Fujiwara, K., Hata, H., Takahashi, H., 2008. Deformation and fragmentation behaviour of exploded metal cylinders and the effects of wall materials, configuration,explosive energy and initiated locations. International Journal of Impact Engineering 35, 1578–1586.

[15] Janiszewski, J., 2012. Ductility of selected metals under electromagnetic ring test loading conditions. International Journal of Solids and Structures 49, 1001–1008.

[16] Jeanson, A.C., Bay, F., Jacques, N., Avrillaud, G., Arrigoni, M., Mazars, G., 2016. A coupled experimental/numerical approach for the characterization of material behaviour at high strain-rate using electromagnetic tube expansion testing. International Journal of Impact Engineering 98, 75 – 87.

[17] Kipp, M.E., Grady, D.E., 1985. Dynamic fracture growth and interaction in one dimension. Journal of the Mechanics and Physics of Solids 33, 399–415.

[18] Kipp, M.E., Grady, D.E., Swegle, J., 1993. Numerical and experimental studies of high-velocity impact fragmentation. International Journal of Impact Engineering 14, 427 – 438.

[19] Mercier, S., Granier, N., Molinari, A., Llorca, F., Buy, F., 2010. Multiple necking during the dynamic expansion of hemispherical metallic shells, from experiments to modelling. Journal of the Mechanics and Physics of Solids 58, 955–982.

[20] Mercier, S., Molinari, A., 2003. Predictions of bifurcations and instabilities during dynamic extensions. International Journal of Solids and Structures 40, 1995–2016.

[21] Mercier, S., Molinari, A., 2004. Analysis of multiple necking in rings under rapid radial expansion. International Journal of Impact Engineering 30, 403–419.

[22] Mott, N.F., 1943a. A Theory of the fragmentation of shells and bombs.

[23] Mott, N.F., 1943b. Fragmentation of shell casings and the theory of rupture in metals.

[24] Mott, N.F., 1943c. Fragmentation of shells: a theoretical formula for the distribution of weights of fragments.

[25] Mott, N.F., 1947. Fragmentation of shell cases. Proceedings of the Royal Society of London. Series A. Mathematical and Physical Sciences 189, 300–308.

[26] Mott, N.F., Linfoot, E.H., 1943. A theory of fragmentation.

[27] Needleman, A., 1991. The effect of material inertia on neck development. In: Yang, W.H. (Ed.), Topics in Plasticity. AM Press, Ann Arbor, MI , 151–160.

[28] Niordson, F.L., 1965. A unit for testing materials at high strain rates. Experimental Mechanics 5, 29–32.

[29] N'souglo, K., Rodríguez-Martínez, J.A., Cazacu, O., 2020. The effect of tension-compression asymmetry on the formation of dynamic necking instabilities under plane strain stretching. International Journal of Plasticity , 102656.

[30] N'souglo, K.E., Srivastava, A., Osovski, S., Rodríguez-Martínez, J.A., 2018. Random distributions of initial porosity trigger regular necking patterns at high strain rates. Proceedings of the Royal Society A: Mathematical, Physical and Engineering Sciences 474, 20170575.

[31] Pandolfi, A., Krysl, P., Ortiz, M., 1999. Finite element simulation of ring expansion and fragmentation: The capturing of length and time scales through cohesive models of fracture. International Journal of Fracture 95, 297–297.

[32] Rodríguez-Martínez, J.A., Vadillo, G., Fernández-Sáez, J., Molinari, A., 2013a. Identification of the critical wavelength responsible for the fragmentation of ductile rings expanding at very high strain rates. Journal of the Mechanics and Physics of Solids 61, 1357–1376.

[33] Rodríguez-Martínez, J.A., Vadillo, G., Zaera, R., Fernández-Sáez, J., 2013b. On the complete extinction of selected imperfection wavelengths in dynamically expanded ductile rings. Mechanics of Materials 60, 107–120.

[34] Rusinek, A., Zaera, R., 2007. Finite element simulation of steel ring fragmentation under radial expansion. International Journal of Impact Engineering 34, 799–822.

[35] Singh, M., Suneja, H., Bola, M., Prakash, S., 2002. Dynamic tensile deformation and fracture of metal cylinders at high strain rates. International Journal of Impact Engineering 27, 939 – 954. Seventh Internation Symposim on Structural Failure and Plasticity.

[36] Sørensen, N.J., Freund, L.B., 2000. Unstable neck formation in a ductile ring subjected to impulsive radial loading. International Journal of Solids and Structures 37, 2265–2283.

[37] Strano, G., Hao, L., Everson, R.M., Evans, K.E., 2013. Surface roughness analysis, modelling and prediction in selective laser melting. Journal of Materials Processing Technology 213, 589 – 597.

[38] Tang, Y., Loh, H., Wong, Y., Fuh, J., Lu, L., Wang, X., 2003. Direct laser sintering of a copper-based alloy for creating three-dimensional metal parts. Journal of Materials Processing Technology 140, 368 – 372. Proceedings of the 6th Asia Pacific Conference on materials Processing.

[39] Tuğcu, P., 1996. Inertial effects in ductile failure of cylindrical tubes under internal pressure. International Journal of Impact Engineering 18, 539–563.

[40] Tuğcu, P., 2003. Instability and ductile failure of thin cylindrical tubes under internal pressure impact. International Journal of Impact Engineering 28, 183–205.

[41] Vadillo, G., Rodríguez-Martínez, J.A., Fernández-Sáez, J., 2012. On the interplay between strain rate and strain rate sensitivity on flow localization in the dynamic expansion of ductile rings. International Journal of Solids and Structures 49, 481–491.

[42] Vaz-Romero, A., Mercier, S., Rodríguez-Martínez, J.A., Molinari, A., 2019. A comparative study of the dynamic fragmentation of non-linear elastic and elasto-plastic rings: The roles of stored elastic energy and plastic dissipation. Mechanics of Materials 132, 134 – 148.

[43] Vaz-Romero, A., Rodríguez-Martínez, J.A., Mercier, S., Molinari, A., 2017. Multiple necking pattern in nonlinear elastic bars subjected to dynamic stretching: The role of defects and inertia. International Journal of Solids and Structures 125, 232–243.

[44] Vaz-Romero, A., Rotbaum, Y., Rodríguez-Martínez, J.A., Rittel, D., 2016. Necking evolution in dynamically stretched bars: New experimental and computational insights. Journal of the Mechanics and Physics of Solids 91, 216–239.

[45] Xue, Z., Vaziri, A., Hutchinson, J.W., 2008. Material aspects of dynamic neck retardation. Journal of the Mechanics and Physics of Solids 56, 93–113.

[46] Zaera, R., Rodríguez-Martínez, J.A., Vadillo, G., Fernández-Sáez, J., Molinari, A., 2015. Collective behaviour and spacing of necks in ductile plates subjected to dynamic biaxial loading. Journal of the Mechanics and Physics of Solids. 85, 245–269.

[47] Zhang, H., Ravi-Chandar, K., 2006. On the dynamics of necking and fragmentation - I. Real-time and post-mortem observations in Al 6061-O. International Journal of Fracture 142, 183–217.

[48] Zhang, H., Ravi-Chandar, K., 2010. On the dynamics of localization and fragmentation - IV. Expansion of Al 6061-O tubes. International Journal of Fracture 163, 41–65.

[49] Zheng, X., N'souglo, K.E., Rodríguez-Martínez, J.A., Srivastava, A., 2020. Dynamics of necking and fracture in ductile porous materials. Journal of Applied Mechanics 87.

[50] Zhou, F., Molinari, J.F., Ramesh, K.T., 2006. An elasto-visco-plastic analysis of ductile expanding ring. International Journal of Impact Engineering 33, 880–891.